UNIVERSITY OF CALIFORNIA
RIVERSIDE

Plasma Synthesis of Silicon Carbide Nanoparticles and Applications for Plasmonics and Thermoelectrics

A Dissertation submitted in partial satisfaction
of the requirements for the degree of

Doctor of Philosophy

in

Materials Science & Engineering

by

Devin Thomas Coleman

March 2019

Dissertation Committee:

Prof. Lorenzo Mangolini, Chairperson
Prof. Alex Greaney
Prof. Chen Li

The Dissertation of Devin Thomas Coleman is approved:

Committee Chairperson

University of California, Riverside

Acknowledgments

Firstly, I would like to sincerely thank my Ph.D. advisor, Professor Lorenzo Mangolini, for his support, mentorship, and guidance. Additionally, I would like to recognize Dr. Sabah Bux, who has been in all but name my second advisor throughout my Ph.D. My journey through my Ph.D. has been as much a personal transformation as professional. For this, I am grateful to all of the friends and colleagues I have met along the way. Although they are too many to name, I am especially grateful to Christian Roach, Nicholas Derimow, Trevor Clark, Noam Hart, Austin Woodard, and Sina Shahrezai for all the experiences we have shared and all times I have leaned on them, in both my professional and personal lives. Lastly, my deepest gratitude goes to my parents, Michael and Peri Coleman, my siblings, Ryan Coleman and Tori Coleman, my grandfather, Ted Black, and my wife, Ece Coleman. They are all, in their own different ways, responsible for making me the person and scientist I am today. I would not be where I am without their unwavering love and support for both me and my passions.

The text of this dissertation, in part or in full, is reprinted of the material as it appears in the following journal papers:

Chapter 2: D. Coleman & T. Lopez, O. Yasar-Inceoglu, and L. Mangolini, "Hollow silicon carbide nanoparticles from a non-thermal plasma process", Journal of Applied-Physics, 117, 193301 (2015)

Chapter 3: D. Coleman, T. Lopez, S. Exarhos, M. Mecklenburg, and S. Bux & L. Mangolini "Thermoelectric performance of silicon with oxide nanoinclusions", Materials Research Letters, 6:8, 419-425, 2018

Chapter 4: D. Coleman & A. Hosseini, and S. Bux, A. Greaney, L. Mangolini, "Seebeck enhancement by electron energy filtering in SiC/Si nanocomposites", *in preperation*

Chapter 5: D. Coleman and L. Mangolini, "Plasmonic core-shell silicon carbide-graphene nanoparticles", *in preparation*

Dedicated to:

My wife, Ece

My parents, Michael and Peri

My grandfather, Ted.

ABSTRACT OF THE DISSERTATION

Plasma Synthesis of Silicon Carbide Nanoparticles and Applications for Plasmonics and Thermoelectrics

by

Devin Thomas Coleman

Doctor of Philosophy, Graduate Program in Materials Science & Engineering
University of California, Riverside, March 2019
Prof. Lorenzo Mangolini, Chairperson

This work intends to expand upon the materials and applications achievable by non-thermal plasma processing, as well as to further the understanding of thermal and electrical transport in bulk silicon nanostructures, with an emphasis on optimizing these structures for thermoelectric performance. The focus of this work is to develop and characterize novel systems for the synthesis of nanoparticles and nanostructures.

These particles will be used to create high performance thermoelectric materials from inexpensive, abundant materials, and develop knowledge that will aid in thermal engineering of future materials. Non-thermal plasma synthesis and processing will be utilized to produce silicon and silicon carbide nanoparticles with narrow size distributions, tunable size, and controllable surface composition and morphology. The synthesis and investigation of novel nanostructures exhibiting surface plasmon resonance will be presented.

The compositing and sintering of dissimilar nanomaterials via hot pressing to create novel silicon bulk nanostructures will be demonstrated. Such samples are extensively characterized and modeled to correlate their thermoelectric performance to physical struc-

ture (e.g. grain size, porosity, inclusions) and elucidate the role of these structures on electrical and thermal transport.

Contents

List of Figures

Chapter 1

Introduction

1.1 Background - Plasma Synthesis of Nanoparticles

Plasma synthesis of nanoparticles originated as an unwanted byproduct during development of plasma processing for thin film deposition in the semiconductor industry. In such unoptimized systems, the formation of nanoparticles interfered with deposition of conformal thin films. These so called "dusty plasmas" were later found to be of interest, and optimized for the production of free-standing nanoparticles.

Since then, the synthesis of nanoparticles from gaseous precursors (e.g. silane, acetylene) as well as evaporated liquid and solid precursors (e.g. chlorides of silicon, germanium, titanium) through non-thermal plasma synthesis has been explored. The use of such systems to produce silicon nanoparticles has been optimized to provide precise control of crystallinity, surface termination (e.g. hydrogen, chlorine, organic ligands) and particle size. Typical particle sizes range from 2-30nm mean diameter with standard deviations around $\sim$20% of average particle diameter.

In the case of silicon nanoparticles synthesized from silane, the nucleation is driven by the decomposition and reaction of SiH_4 molecules to form larger molecules. This process yields small clusters of silicon with Si-H surface termination. The reaction continues by replacing the hydrogen bonds with SiH_x species. Because the frequency of particle-electron interaction is significantly higher than that of particle-ion, these particles develop a unipolar negative charge that causes them to begin to repel each other as they grow, leading to a self-limited growth and small final particle sizes with narrow distributions. [24]

These reactors are not limited to only silicon. Similar systems have been developed for the synthesis of other semiconducting materials such as germanium, titanium nitride, zirconium nitride, and silicon carbide, as well as metallic particles such as nickel and aluminum.

1.2 Background - Thermoelectrics

Thermoelectricity is the direct conversion of energy between electricity and heat. Thermoelectric generators have been heavily utilized for decades in space exploration as reliable, solid state power sources with very long lifetimes. Increasingly, they are becoming attractive for terrestrial applications such as waste heat recovery in automobiles or industrial facilities, solid-state temperature control and refrigeration, and self-powering wearable medical devices. The key to realizing these applications is in improving the efficiency of bulk thermoelectrics. The efficiency of a thermoelectric material is directly related to its dimensionless figure of merit, ZT, defined as $ZT=(\sigma S^2 T)/k$, where σ is the electrical conductivity, S is the Seebeck coefficient, k is the thermal conductivity, and T is the temperature. Thus,

the ideal thermoelectric material is one which exhibits "electron crystal, phonon glass" behavior, and electrons travel much more freely than heat carrying phonons. [1]

Initial thermoelectric performance was dominated by rare earth tellurides such as Bi_2Te_3 and PbTe, producing ZTs of $\sim$1. This performance was soon approached by alloys of polycrystalline SiGe alloys, which are still used in Radioisotope Thermoelectric Generators for modern day space exploration. [2, 3] Later studies on nanoscale materials, such as thin films or nanowires, indicated that electrical and thermal conductivities could be effectively decoupled through introduction of nanoscale features to enhance ZT. [4] Bux et al demonstrated the effects of nanoscale grains on thermal conductivity in bulk silicon through sintering of nanopowders produced by high energy ball milling, achieving a record ZT of 0.7 without the addition of expensive or rare elements. [5] However, modeling and low temperature thermal conductivity measurements have demonstrated that grain boundary scattering alone does not scatter low-frequency phonons, which can carry a great deal of heat even at high temperatures. [6] Studies on thin films featuring patterned quantum dots and superlattice structures have demonstrated their ability to further depress thermal conductivity, as well as improve electrical performance through the enhancement of power factor. [7–9] However, these processes are not scalable to create the bulk materials necessary to enable their realization in thermoelectric modules. The thermoelectric branch of this study aims to develop novel processes for engineering bulk nanostructured materials containing superlattice-like nanoinclusions. The supporting technology for the production of these nanoinclusions is non-thermal plasma nanoparticle synthesis.

Chapter 2

Non-thermal Plasma Synthesis of Silicon Carbide Nanoparticles

2.1 Introduction

Silicon carbide is a relevant material for several applications including high-power electronics, [10] optoelectronic applications, [11–13] catalysis, [**?**,14] and the development of microelectromechanical systems. [15,16] Such interest is due to its unique properties in terms of mechanical hardness and fracture toughness, high chemical stability, high charge carrier mobility, and good thermal transport properties. The capability of producing high-quality silicon carbide nanoparticles could provide new opportunities in all of the areas mentioned above. Several approaches have been proposed for the production of silicon carbide nanoparticles, such as laser-induced pyrolysis of silane-methane mixtures, [17] dissociation of silicon and carbon precursors in a thermal plasma followed by expansion in a supersonic jet, [18,19]

and direct nucleation of silicon carbide nanoparticles in low-pressure non-thermal plasmas containing a silane-methane mixture. [20,21] In particular, this last approach has led to the production of amorphous silicon carbide particles. On the other hand, continuous flow non-thermal plasma reactors have been shown to be compatible with the high-yield production of nanocrystals of high melting point materials such as silicon. [22–25] Nanoparticles of even higher melting point materials, such as silicon carbide nanocrystals and carbon nanodiamonds, have recently been produced using atmospheric pressure microplasmas. [26] Finally, the presence of beta-silicon carbide has been reported for a two-step process involving the non-thermal plasma synthesis of silicon particles and their non-thermal plasma-initiated in-flight coating with carbon using acetylene as precursor. [27]

These reports have provided the original motivation for our study on the non-thermal plasma synthesis of silicon carbide nanoparticles. We have developed a two-step process for the synthesis and in-flight carbonization of silicon nanocrystals. We have found that silicon particles produced in a first non-thermal plasma step can be rapidly converted into beta silicon-carbide nanocrystals by exposing them to a methane-containing non-thermal plasma. The carbonization process occurs in-flight and over a total time scale of the order of 100 ms. Under the appropriate conditions, the carbonization process is associated with the formation of hollow silicon carbide nanoparticles. An analysis of the diffusion kinetics in the silicon-carbon binary system suggest that the diffusion of carbon into the silicon core is substantially faster than the out-diffusion of silicon towards a carbon-rich outer region, ruling out the nanoscale Kirkendall effect as a possible mechanism leading to the hollow structure. [28] The lattice volume expansion upon nucleation of silicon carbide

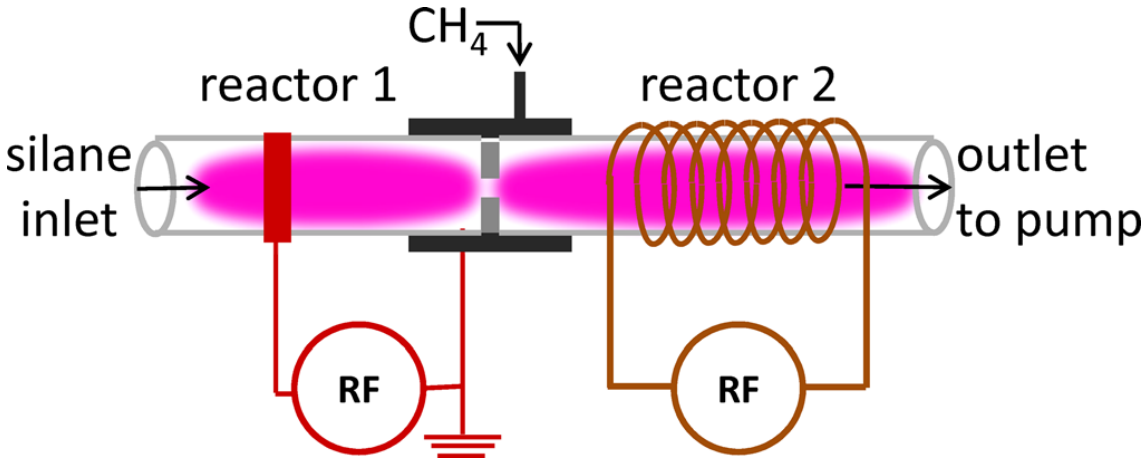

Figure 2.1: Schematic of the two-step plasma reactor used in this study

in the outer shell of the silicon particle is a much more likely mechanism leading to the final hollow structure. The analysis of the energetics of the carbonization reaction reveals that the formation of silicon carbide is a highly exothermic reaction, which heats the particle to a temperature much higher than that of the background gas. This energy release accelerates the silicon-to-silicon carbide conversion process, which reaches completion on a time scale much shorter than the nanoparticle residence time in the reactor.

2.2 Experimental

In figure 2.1, we show a schematic of the experimental apparatus, which has been specifically optimized for the synthesis of silicon nanoparticles and for their in-flight carbonization. The first stage of this reactor is similar to the one previously described in Refs. [22] and [29] and composed of a 2.54 cm outer diameter quartz tube; 100 sccm of an argon-silane mixture is flown at the inlet of the first stage. The silane concentration is 1.37% by volume. The pressure in the first plasma is 6 Torr (800 Pa). The powered electrode is

composed of a copper ring placed at a distance of 7 cm from the downstream metal flange. During operation, the nonthermal plasma is coupled to the downstream flange, which is electrically grounded. The second stage of this reactor is also composed of a 2.54 cm diameter quartz tube. The second non-thermal plasma is generated using a coil electrode with a length of 25 cm. A 1mm diameter orifice separates the first and second stages of the reactor, and the pressure in the second stage is automatically controlled using a butterfly valve, and it is equal to 1 Torr (130 Pa). Two radio frequency (13.56 MHz) power supplies are used to strike and sustain the discharges. The carbon precursor used in this study is methane, whose inlet is placed immediately downstream of the orifice separating the two reactors. The methane flow rate is 5 sccm. Visual inspection confirms that during operation, the second plasma also couples to the metal flange assembly that separates the reactors. As a consequence, the silicon particles nucleated in the first stage are accelerated through the orifice and immediately injected into the second plasma during which the carbonization process takes place. A metal mesh is used as a filter to collect the particles downstream of the plasma volume. A variety of materials characterization techniques have been used to analyze the produced powder. X-ray diffraction (XRD) has been performed on a PANalytical EMPYREAN instrument with CuKa source. Transmission electron microscopy (TEM) has been performed on either a TECNAI T12 and on a Philips CM300. Raman has been performed on a Horiba LabRam system with a 532 nm laser source.

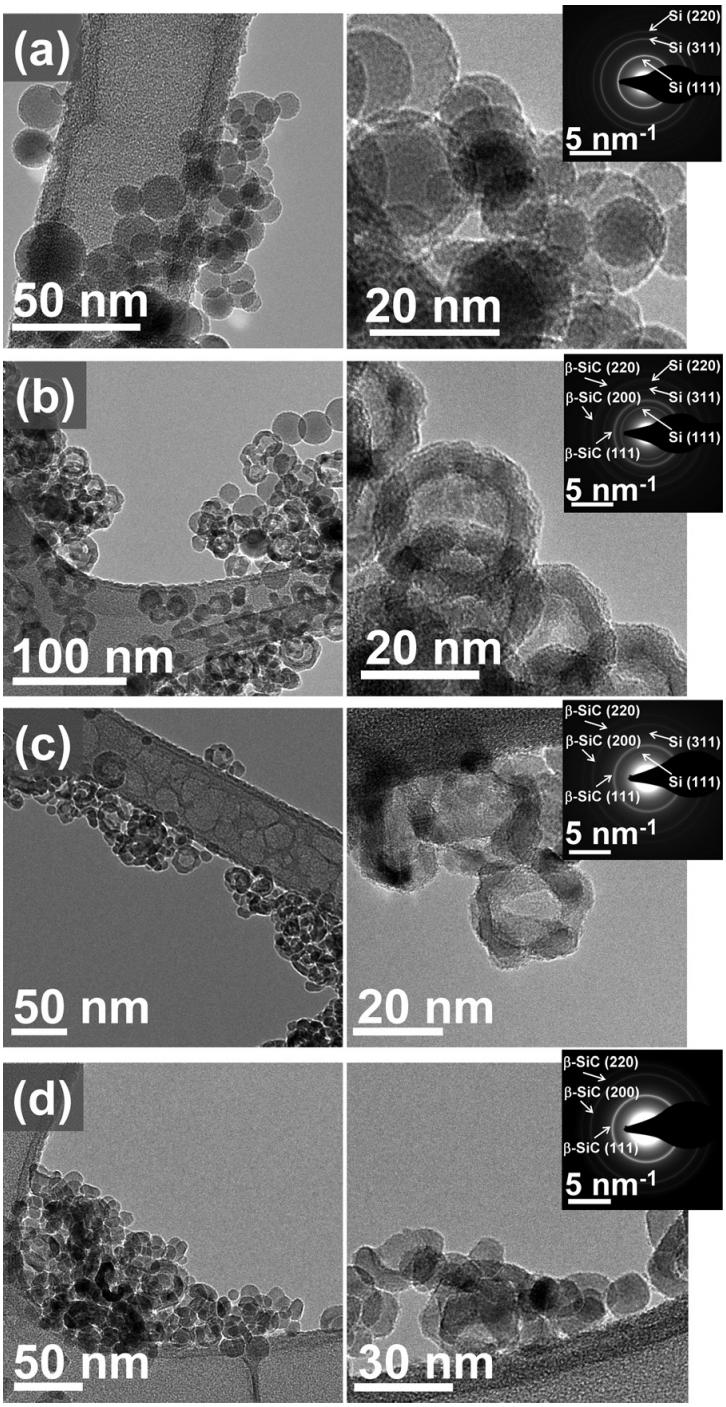

Figure 2.2: Results of TEM analysis of the produced powders as a function of input power in the second plasma. Lower magnification images are shown on the left side, while higher magnification images are on the right. Selected area diffraction patterns for each sample are also shown as an inset of the higher magnification image. The samples have been treated using the following electrical input powers to the second reactor: (a) 12 W, (b) 20 W, (c) 30 W, and (d) 40 W.

2.3 Results

In Figure 2.2, we summarize the results from TEM analysis. For this series of images, the power in the first reactor is constant and equal to 100 W, while the power supplied to the second plasma is varied between 8W and 40 W. In Figure 2.2a, we show lower and higher magnification micrographs of the silicon particles processed in the second stage with a power of 12 W. The particles have a fairly broad size range between 10 nm and 30 nm. This is due to the long residence time in the first stage of the system, i.e., in the silicon nanoparticle production step. The residence time is 250 ms, based on the flow velocity and the length of the first plasma. The higher magnification image on the right side suggests the particles are spherical. The selected area diffraction pattern confirms that these particles are composed of silicon with diamond structure, since the pattern shows clear contribution from the (111), (311), and (220) reflections of crystalline silicon. At the higher power of 20W (Figure 2.2b), it is possible to observe a drastic change in the particle morphology: while some spherical particles are still present, most particles appear to have a core-shell structure. The low contrast from the core of these particles, which is clear in the higher magnification image, suggests that these particles are hollow. The selected area diffraction still shows contribution from silicon, although additional rings which can be indexed to the (111), (200), and (220) planes of beta silicon carbide (β-SiC) are distinguishable. At even higher power (30 W, Figure 2.2c), it is possible to observe additional morphological evolution. The larger spherical particles are now absent, while the shape of the hollow particles becomes more irregular. This morphological change, likely driven by a reduction in specific surface area, ultimately leads to the breakdown of the

hollow spherical structure. The selected area for this power in the second plasma reactor indicates that a higher degree of conversion from silicon to silicon carbide is obtained, since the contribution from the crystalline silicon structure is barely distinguishable. The breakdown of the hollow spherical structure is obvious for an input power of 40W (Figure 2.2d). None of the hollow spheres survive and smaller particles (15 nm) with irregular shapes are now observed. It is interesting to point out that these particles are actually smaller than the original silicon particles that have undergone carbonization. The selected area diffraction pattern suggests that the conversion of silicon to silicon carbide is complete.

The XRD spectra for several samples produced at increasing RF power supplied to the second plasma are shown in Figure 2.3a. Peaks from the following planes of silicon are distinguishable for the sample produced at low power: (111) at 28.47°, (220) at 47.35°, (311) at 56.18°, (400) at 69.2°, and (331) at 76.4°. The (111), (220), and (311) planes of β-SiC (35.68°, 60.04°, and 71.84°, respectively) are detected at higher power. The onset of β-SiC formation occurs around 18W of input power in the second discharge, and the conversion is complete at 25 W. A summary of the conversion process is shown in Figure 2.3b in which we plot the ratio between the area under the beta silicon carbide peaks and the total area under all peaks appearing in the XRD spectra, i.e., the crystalline fraction of SiC in the sample. To summarize, increasing the electrical power input into the second plasma leads first to the conversion of the silicon particles into β-SiC nanoshells. As the input power is increased, the morphology of the hollow particles is destabilized, leading to their breakdown into smaller particles that maintain the β-SiC structure.

Higher magnification images for the same conditions shown in Figure 2.2b are

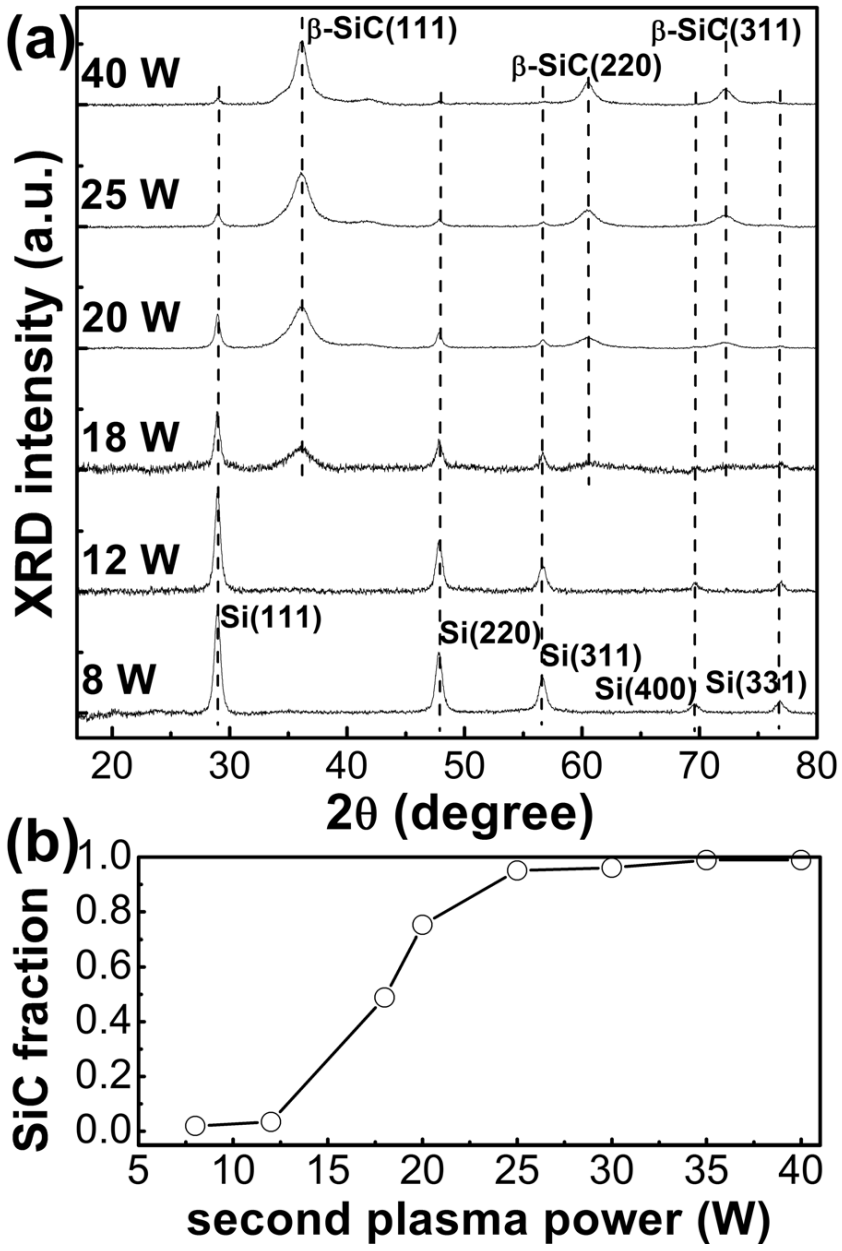

Figure 2.3: (a) XRD of the produced powders as a function of RF power input to the second discharge. (b) Crystalline fraction of SiC also as a function of RF power input to the second discharge.

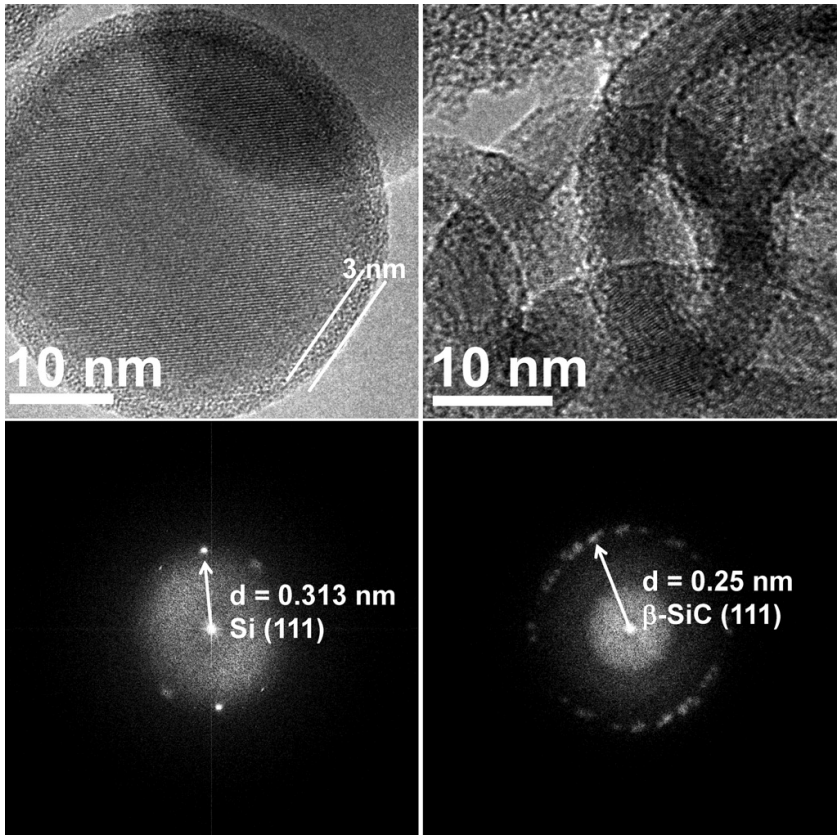

Figure 2.4: (Left) Spherical silicon nanoparticles produced at a power input to the second discharge of 20 W. (Right) Hollow silicon carbide nanoparticles produced under the same conditions. The corresponding FFT images are shown below each micrograph.

presented in Figure 2.4. Figure 2.2b suggests that for this power input the sample has a structurally bimodal distribution, i.e., the particles are either spherical silicon crystals (Figure 2.4, left image) or hollow silicon carbide particles (Figure 2.4, right image). The fast Fourier transform analysis (FFT) of these two images confirms that the solid particles have a crystalline silicon structure, since the measured lattice spacing is 0.31 nm, consistent with the spacing of the (111) planes of diamond silicon. The lattice spacing for the hollow particles is 0.25 nm, matching the (111) spacing of β-SiC. The higher magnification image on the left also suggests that the solid silicon particle is coated with a 3 nm amorphous layer, which is too thick to be a native oxide. A native oxide layer, based on our previous experience, is 1 nm thick for crystalline silicon particles. [22] We have performed Raman characterization to further investigate the nature of the amorphous shell observed in Figure 2.4. The results from Raman characterization are shown in Figure 2.5 for a sample which has not been exposed to the carbonization process (0% SiC), for a sample treated with 18W of power input in the second plasma (50% SiC volume fraction), and for a fully carbonized sample (30W of power input in the second plasma). The spectra have been normalized to their maximum value for comparison. For the non-carbonized sample (bottom spectrum), the only apparent feature comes from the Si-Si transverse optical phonon (TO) at 519 cm^{-1}. The slight shift to lower wavenumber compared to the bulk value of 521 cm^{-1} is due to size effects. [30] For samples with roughly a 50% volume fraction of silicon carbide (corresponding to Figure 2.2b, the Si-Si feature is still present, but the spectrum is rich with additional features including broad peaks centered at 440 cm^{-1}, 1360 cm^{-1}, and 1530 cm^{-1}, which are attributed to amorphous carbon. [31, 32] Increased intensity around 800–1000

cm^{-1} range can be attributed to silicon carbide, [33, 34] although the broad appearance of these features is typically observed in amorphous silicon carbide. [34] Sharp peaks at 795 cm^{-1} and 950 cm^{-1} are generally observed for crystalline β-SiC. [35] In addition, the peaks at 650 cm^{-1} and in the 1000–1200 cm^{-1} range cannot be easily assigned to features due to either carbon or amorphous carbide. A more detailed investigation of the Raman signature of nanostructured SiC is left for a future contribution. For a fully carbonized sample, we observe a spectrum that is very similar to the one for the partially carbonized one with the difference that the Si-Si contribution has disappeared. Raman suggests that the carbonization of the silicon particles is preceded by the growth of an amorphous carbon layer around them, as suggested by the TEM image shown in Figure 2.4. It also indicates that once the silicon particles have been fully converted to silicon carbide, an amorphous carbon phase may still be present. This is reasonable, since the methane flow rate is 5 sccm, largely exceeding the 1.37 sccm of silane fed into the first stage of the reactor. We can, therefore, conclude that the silicon-to-silicon carbide conversion is limited by the kinetics of the carbonization process and not by the availability of carbon (i.e., it is not mass limited).

To summarize, silicon nanocrystals in the 15–30 nm size range are produced in the first non-thermal reactor. Our previous work on the characterization of silane-containing nonthermal plasmas suggests that the silane precursor is fully consumed in the first stage of the process. [36] The silicon nanocrystals are then exposed to the second plasma to which methane is added. Exposure to the methane-containing plasma leads to first (a) the growth of an amorphous carbon film around the silicon particles (as confirmed by higher magnification images in Figure 2.4 and by Raman in Figure 2.5), followed by (b)

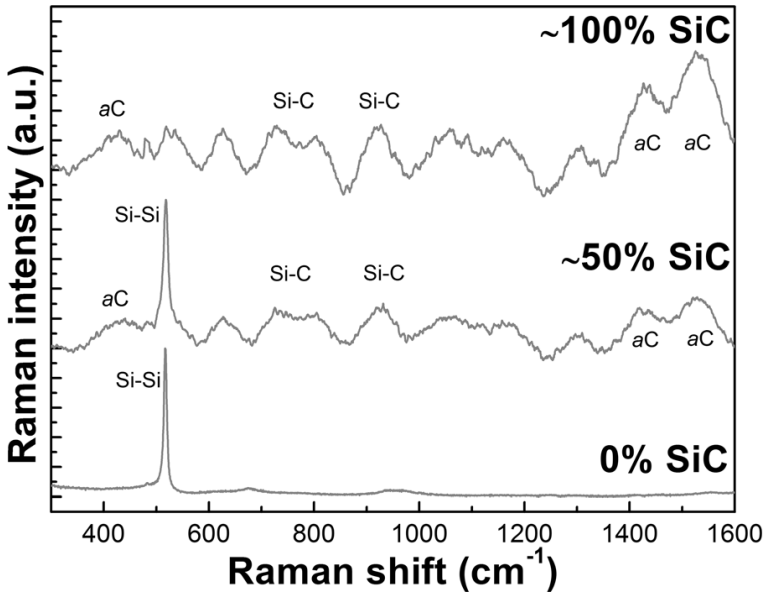

Figure 2.5: Raman Spectra for samples with different fractions of β-SiC.

the formation of beta silicon carbide nanoshells, and (c) the destabilization of the hollow shell structure, which ultimately results in the formation of solid (as opposed to hollow) silicon carbide nanoparticles with diameters smaller than the original silicon particles. A more detailed description on this process, in particular, with respect to the kinetics of carbon diffusion in the silicon particle and the nanoparticle morphology is presented in the following text.

2.4 Discussion

Hollow silicon carbide nanostructures have been already observed for the case of nanowires [37] and nanoparticles [38] as well. Hollow cores have been proposed to occur as a result of the out-diffusion of silicon towards the carbon-rich outer layer in a process identical to the Kirkendall nanoscale effect: [28] hollow structures are obtained when the diffusion

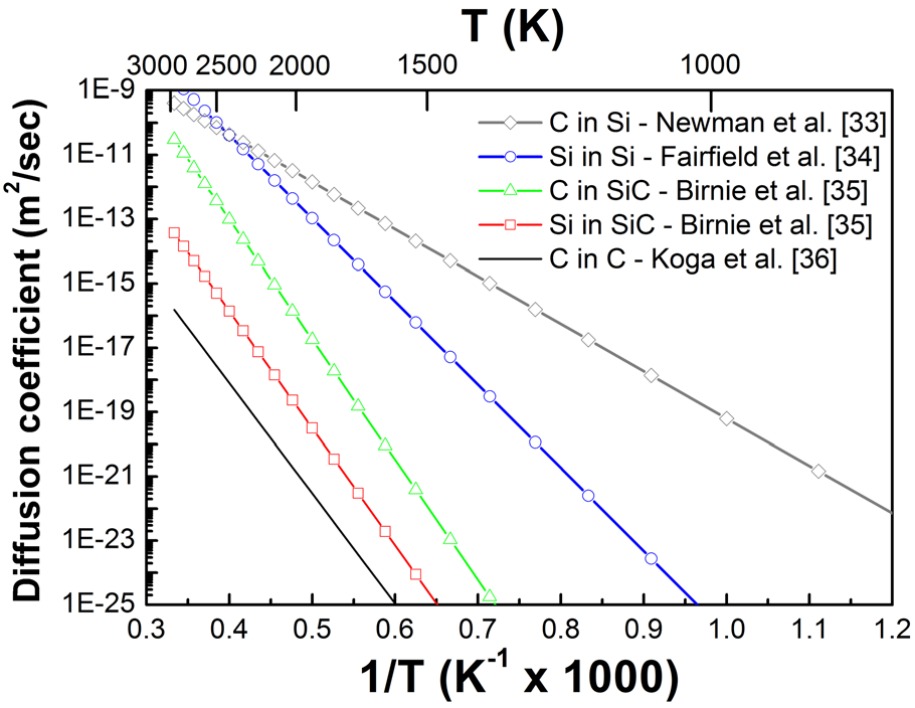

Figure 2.6: Diffusion coefficients as a function of temperature in the Si-C system.

kinetics for the core element in the shell material is faster than that of the shell element in the core material. For such process to occur in the Si-C system, the diffusion coefficient of silicon in carbon would have to be faster than the diffusion of carbon in silicon. Our review of the literature on diffusion kinetics in the Si-C system clearly indicates that this is not possible. In Figure 2.6, we plot the diffusion coefficient as a function of temperature for carbon diffusion in silicon, [39] silicon self-diffusion, [40] silicon and carbon diffusion in silicon carbide, [41] and carbon self-diffusion. [42] We could not find data in the literature on the diffusion kinetics of silicon into carbon. Experimental measurement for the diffusion of various elements in amorphous carbon [43] suggests that even for small atoms such as hydrogen and deuterium, diffusion is insignificant below 800 °C (1100 K). Metals such as tungsten, copper, and silver do not diffuse below 1000 °C (1300 K). In addition, the large

atomic radius of silicon compared to carbon (110 pm vs. 70pm, respectively [44]) and the fact that even the self-diffusion of carbon is vacancy mediated [42] leads us to conclude that carbon diffuses much more rapidly into silicon than silicon in carbon. We should also point out that the diffusion of carbon in silicon carbide is also almost two orders of magnitude larger than that of silicon in silicon carbide. [41]

These considerations rule out the Kirkendall effect as a possible explanation for the hollow particle formation. We provide an alternative justification, which is consistent with the observation of hollow SiC nanoparticles. Using bulk density values for silicon and β-SiC (2.33 kg/m^3 and 3.21 kg/m^3, respectively), we find that the molar specific volume of silicon carbide is larger than that of silicon (1.246×10^{-2} m^3/kmol vs. 1.205×10^{-2} m^3/kmol, respectively). This implies that a 3.38% volume expansion accompanies the carbonization of silicon and the formation of the beta-silicon carbide lattice. This effect is important in spherical coordinates, since the carbonization process proceeds radially inward from the carbon source, i.e., the plasma-deposited amorphous carbon shell. We have made the assumption that the outer 4 nm thick silicon shell is first saturated with carbon and converted into silicon carbide. The 4 nm thickness is motivated by the Scherrer analysis of the XRD pattern at the early onset of the carbonization (see Figure 2.3, 18W spectrum). Under the simplifying assumption of azimuthal and polar symmetry (i.e., an outer shell with uniform thickness is converted into silicon carbide) and under the assumption of uniform volume expansion upon nucleation of silicon carbide in the outer shell of the silicon particle, the inner and outer diameters of the silicon shell participating in the nucleation process expand from 8.54 nm and 12.5 nm to 8.64 nm and 12.64 nm, respectively. Although this

appears to be a minor change, conservation of silicon volume in the spherical geometry implies that a 5.4 nm diameter void must form at the center of the silicon core. After this initial stage of carbonization, the SiC volume fraction is 68%. Carbon then diffuses through the SiC shell and reacts with the silicon core, leading to complete conversion of Si to β-SiC. The kinetics of diffusion through the SiC layer are enhanced by the rapid heating of the particle induced by the release of the enthalpy of formation of silicon carbide, which will be covered in greater detail later in the manuscript. The diffusion of carbon through the SiC layer is much faster than the diffusion of silicon through the same layer (see Figure 2.6), supporting the conclusion that additional SiC forms at the interface between the SiC shell and the silicon core, and not at the interface between the SiC shell and the outer carbon-rich layer. Under the assumption of continuous expansion of the silicon lattice during carbonization, we find that at the end of the carbonization process (100% silicon carbide volume fraction), the particle has an inner diameter of 11 nm and an outer diameter of 26 nm. This is in reasonable agreement with TEM observation. It is clear that the assumption of uniform nucleation of silicon carbide in a constant thickness spherical shell is not realistic, since TEM data confirms that the silicon carbide nanoshell is polycrystalline. This implies that multiple silicon carbide nucleation events take place in each particle at the early stage of the carbonization process. A more complex numerical approach is going to be needed to achieve a more realistic model, and such effort goes beyond the scope of this contribution. Nevertheless, for simplicity, we propose to model the silicon-to-silicon carbide conversion proceeds as a two-step process involving first, the inward diffusion of carbon into the silicon particle (which we will refer to as the incubation phase) followed by the nucleation of a

silicon carbide outer shell (nucleation phase) and by the growth of the silicon carbide phase (propagation phase). This simplified approach is capable of predicting the formation of particles with a hollow morphology.

The strong temperature dependence of the diffusion coefficients indicates that knowledge of the nanoparticle temperature is necessary to investigate the kinetics of the process under consideration. This can be done by solving for the transient nanoparticle energy balance during the carbonization process

$$C_p \cdot \frac{dT_{particle}}{dt} = G_1 + G_2 - L \tag{2.1}$$

where $T_{particle}$ is the particle temperature and C_p is the molar heat capacity of the nanoparticle, which is calculated by accounting for the molar fraction of each component during the process (aC, SiC, and Si) and by using the following values of heat capacities: $C_{p,Si}$=19.789 J/mol K, $C_{p,SiC}$=25.6 J/mol K, and $C_{p,aC}$=6 J/mol K. The energy balance equation is coupled to the solution of the mass diffusion of carbon into the silicon lattice and of the diffusion of carbon through the SiC interlayer. This is necessary to track the particle composition during the process. G_1 is a generic heat source term, which lumps together the contribution from various heating mechanisms such as recombination of ions and excited species at the particle surface, interaction with atomic hydrogen, and reaction with carbon-containing radicals that lead to the growth of a carbon shell. The details of the interaction between the partially ionized gas and the nanoparticles suspended within it are still actively investigated. [36, 45, 46] In this work, we do not focus on such details and we treat the second non-thermal plasma as the heating source that provides the heating term G_1. G_2

is used to account for the energy released during the nucleation and propagation phases, which is equal to the enthalpy of formation of beta silicon carbide (73.223 kJ/mol). [**?**] The latent heat of melting for silicon is also included in G2, since the particle temperature is sufficiently high during the carbonization process to melt the silicon core of the particle. Therefore, the enthalpy of formation of β-SiC is diminished by 50.2 kJ/mol during the SiC nucleation phase. [47] L represents the heat loss to the background gas, calculated as

$$L = \frac{1}{4} \cdot n_{Ar} \cdot S \cdot \sqrt{\frac{8 \cdot k_B \cdot T_{gas}}{\pi \cdot \ m_{Ar}}} \cdot \frac{3}{2} \cdot k_B \cdot (T_{particle} - T_{gas}) \tag{2.2}$$

where n_{Ar} is the density of argon, S is the nanoparticle surface area, k_B is the Boltzmann constant, m_{Ar} is the mass of the argon atom, and T_{gas} is the background gas temperature assumed to be 300 K. The energy balance equation is discretized with a 1 μs time step. This approach allows calculating both the time necessary to observe nucleation of silicon carbide in the outer layer of the silicon particle during the incubation phase, and the temperature history of the particle during the silicon carbide nucleation and propagation phases.

We have analytically solved the 1-D diffusion equation in radial coordinates describing the radial inward flow of carbon into the silicon lattice. A diffusion coefficient for carbon in silicon with a pre-exponential factor of 3.3×10^{-5} m^2/s and an activation energy of 2.92 eV has been used. [39] As initial conditions, the carbon density in the silicon lattice is zero, and there is a chemically abrupt interface between the silicon core and an outer carbon shell. We have made the simplifying assumption of azimuthal and polar symmetry (i.e., one-dimensional problem along the radial direction) and established that nucleation

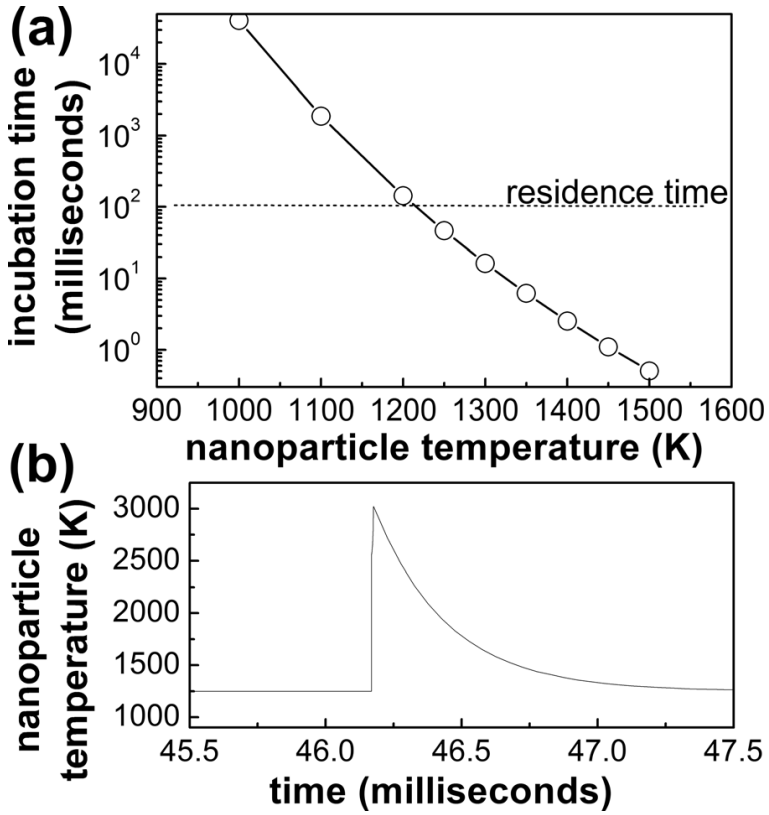

Figure 2.7: (a) Dependence of the incubation time on the nanoparticle temperature. (b) Nanoparticle temperature history during the SiC nucleation and propagation phases.

of silicon carbide occurs when the volume-averaged molar density of carbon in the outer 4 nm silicon shell reaches the molar density of silicon, i.e., when a 1:1 stoichiometric ratio is reached. During this incubation phase, the particle temperature is held constant in time and the term G_2 in Eq. (1) is set to zero, since SiC has not formed yet. This approach allows calculating the time necessary for saturation of the silicon lattice with carbon and for silicon carbide nucleation to occur as a function of nanoparticle temperature. The nanoparticle temperature is thus a free parameter during the incubation phase, and it is varied by arbitrarily adjusting the value of the heating term G_1. The saturation time as a function of nanoparticle temperature is plotted in Figure 2.7a and compared to the nanoparticle residence time in the second plasma. The residence time is calculated based on the flow velocity in the second reactor, and it is found to be 120 ms. Our approach indicates that the nanoparticle must be heated to a temperature higher than 1200K for carbon diffusion to be sufficiently fast to lead to the formation of silicon carbide. Estimates of the nanoparticle temperature in argon-hydrogen low-pressure discharges indicate that the nanoparticle temperature can exceed the gas temperature by several hundreds of degrees. [45,46] In Ref. [36], we have performed an indirect measurement of the nanoparticle temperature based on the kinetics of crystallization of amorphous silicon nanoparticles [47] suspended in an argonhydrogen discharge and found the particle temperature to be 1100 K. The value obtained in this contribution is slightly larger than this value. The discrepancy can be explained in terms of additional heating due to the surface reaction with carbon-containing radicals.

The incubation phase is followed by rapid nucleation of silicon carbide in the outer shell of the particle. During this phase, we have solved for the nanoparticle energy

balance while accounting for the energy released by the formation of β-SiC, diminished by the latent heat of melting of silicon (term G_2). The resulting nanoparticle temperature history for a particle initially heated by the plasma to 1250K is shown in Figure 2.7b. We assume the nucleation process to be faster than the typical time step for integration of the energy balance equation (1 μs), i.e., effectively instantaneous. The sudden nucleation of silicon carbide heats the particle to 2500 K. After the nucleation phase, the rate limiting step becomes the diffusion of carbon through the silicon carbide outer layer. The carbon flux across the silicon carbide shell can be calculated as a function of temperature using a diffusion coefficient with a pre-exponential factor of 86 m^2/s and an activation energy of 7.41 eV (diffusion of C in SiC [41]). We continue to integrate the energy balance assuming that the carbon diffusing through the SiC shell reacts immediately with the silicon core to generate silicon carbide. The process continues till a 100% SiC volume fraction is reached. The incubation time for this temperature is 46 ms. It takes an additional 10 ms for the particle to be fully converted to silicon carbide. Continuous release of the enthalpy of formation for SiC during the propagation phase further increases the particle temperature. A peak temperature of 3000K is reached when carbonization is complete. Afterward, the temperature decays because of conduction to the background gas.

To summarize, our analysis of the process supports the following conclusions: interaction with the plasma induces sufficient nanoparticle heating to achieve nucleation of β-SiC over a time length that is smaller than the particle residence time in the discharge. After this incubation phase, the energy released by the formation of silicon carbide pushes the reaction into a self-propagating regime, which leads to complete structural conversion

on a timescale much shorter than that of the incubation phase. Our prediction of a large difference between the timescales of the incubation stage (tens to hundreds of milliseconds) and of the nucleation-propagation stage (tens of microseconds) is consistent with the experimental data shown in Figure 2.2b: nanoparticles have a structurally bimodal distribution, i.e., they are either silicon carbide nanoshells or crystalline silicon particles with an amorphous carbon shell. Once the incubation phase is complete, the conversion to silicon carbide is very rapid because of the self-enhancing nature of the conversion reaction. This explains why we could not find partially carbonized particles in our TEM analysis (see Figures 2.2b and 2.4).

A confirmation of significant nanoparticle heating in the non-thermal plasma process described in this manuscript is provided by the work of Pai et al., [38] who obtained β-SiC particles in a hot-wall reactor starting from a mixture of silane and methane as precursors only at temperatures exceeding 1200 °C. The same authors also report the formation of hollow β-SiC when the reaction is performed at 1400 °C, although they explain it in terms of fast out-diffusion of silicon from the particle core. In our opinion, geometric considerations related to the volume expansion during carbonization and to the spherical geometry of the system provide a more reasonable explanation to the formation of hollow nanoparticles.

2.5 Conclusions

A process for the formation of silicon nanocrystals and their in-flight carbonization to give β-SiC nanoparticles has been described. By tuning the process parameters, it

is possible to control the nanoparticle morphology from hollow (nanoshells) to solid. An explanation for the formation of hollow structures that does not rely on the Kirkendall effect has been proposed. The analysis of the diffusion kinetics for this system allows for an indirect measurement of the nanoparticle temperature in the plasma, providing further evidence that significant heating occurs during exposure to the non-thermal plasma. This work expands the range of materials that are achievable using non-thermal plasma techniques and confirms their potential as a materials processing tool. It suggests that the synthesis of high-quality nanoparticles of several highly relevant materials (other wide band-gap semiconductors, ceramics, high temperature metal superalloys, etc.) might be possible using non-thermal plasma processes. It also suggests that by carefully engineering such processes, it is possible to achieve control over the particle morphology.

Chapter 3

Thermoelectric Performance of Silicon with Oxide Nanoinclusions

3.1 Introduction

The design and realization of materials for efficient thermoelectric energy conversion has attracted the attention of several research groups. From a fundamental point of view, it requires gaining an intimate understanding of the transport of heat and charge carriers in potentially complex materials. Reducing grain size is an effective way to preferentially increase the phonon over the charge carrier scattering rate, thus improving the thermoelectric figure of merit ZT [1, 48]. Sintering of fine powders has become a common approach for the realization of bulk materials with nanoscale grains [5, 49–51]. Despite this progress, recent reports have suggested that this tactic has limitations. Grain boundaries have been shown to scatter low frequency phonons less efficiently than high frequency

ones [52], and low frequency phonons can carry a significant amount of heat even at high temperatures [53]. There are also unsolved issues with respect of the processing science of such materials. Bulk nanostructured silicon can be obtained by sintering powders produced using a wide range of techniques, such as ball milling [5, 52] and plasma [54–56], and the influence of processing parameters on the transport properties of the resulting bulk samples is far from being fully understood. This contribution focuses on both of these issues. Silicon nanoparticles synthesized using a low temperature plasma-based technique [22, 36] have been hot-pressed into bulk silicon samples. The resulting sample has large grains (micron-sized) and ∼20nm well dispersed silicon oxide precipitates. When compared to a control sample with submicron grains, the sample with nanoinclusions has similar thermal conductivity but higher power factor, leading to a markedly higher thermoelectric figure of merit ZT.

3.2 Experimental

The nanoparticle synthesis technique utilized here is a scaled-up version of the reactor discussed in other contributions [22, 36, 57]. It is composed of a continuous flow non-thermal plasma reactor, tube furnace, and roughing pump, and is capable of producing powder at a rate of the order of grams per hour. The plasma reactor is composed of a 5 cm diameter quartz tube with a 5 cm wide copper electrode wrapped on its outside. The electrode is RF biased at 13.56MHz. For this study, the plasma power is constant and equal to 160W. At the gas inlet, 850 sccm of a mixture of 1.37% silane in argon is flown at a pressure of 3.5 torr. After the plasma synthesis step, the particles are crystalline,

have a hydrogen terminated surface and are 5–10nm in size [29]. Any attempt to sinter the as-produced particles into bulk samples has resulted into extremely brittle samples that shatter during handling. We hypothesize that this is due to the hydrogen surface termination of the particles and the consequent hydrogen-induced embrittlement of the sintered sample. For this reason, we have introduced an in-flight annealing step to thermally remove hydrogen from the particle surface. This is achieved by flowing the particles through a tube furnace with a heated length of 20 cm and kept at 1100°C. This in-flight post-processing step allows us to reproducibly sinter the particles into bulk samples with >99% relative density. Figure 3.1 shows TEM micrographs and particle size distribution of the silicon nanoparticles produced with this approach. The average particle size is 50nm with a standard deviation of 8 nm. They are significantly larger than the 5–10 nm nanoparticles that are typically obtained from non-thermal plasma reactors [22,29,36]. Particle charging, which slows down agglomeration in the plasma reactor [58], is absent once the particles leave the plasma and enter the in-flight annealing step, with the same annealing mechanism enhancing the agglomeration and coalescence kinetics thus leading to rapid growth in size. The particles are collected on a filter downstream of the furnace, sealed in an inert argon atmosphere and transferred to a glove box where they are then mechanically mixed with 2% red phosphorus [59].

We have also sintered silicon powder produced via ball-milling to compare our samples to a more standard structure [5]. Silicon ingot fragments and red phosphorus are sealed in a tungsten carbide vial with 3 tungsten carbide balls of 10 mm diameter in a 50 mL WC vial (Spex industries) and milled in the Spex for 24 hours. It is important to note

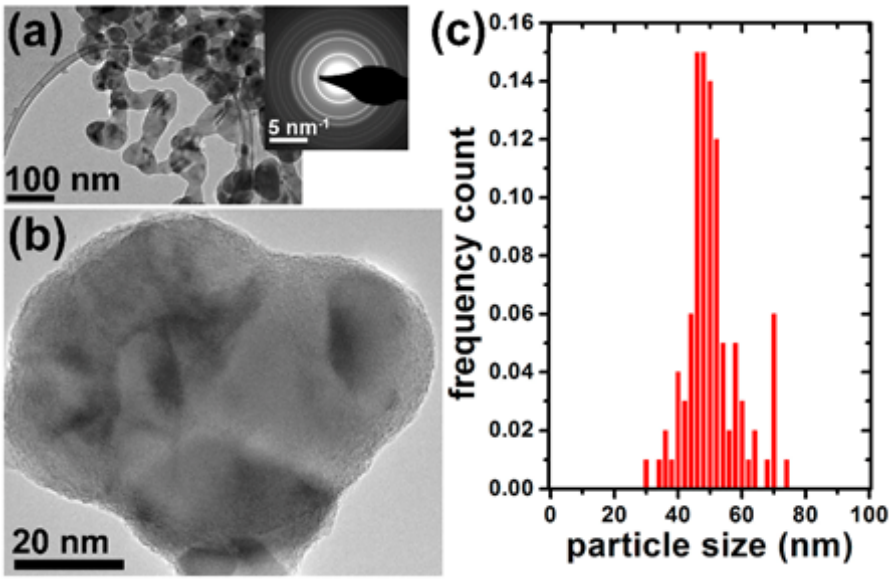

Figure 3.1: Low (a) and high (b) magnification TEM micrographs of the silicon particles produced in our lab. The selected area diffraction pattern is shown in the inset of figure (a). (c) Particle size distribution obtained by the analysis of the TEM micrographs.

that the particles produced with our synthesis technique have significantly larger specific surface area than the ones obtained via ball milling: 41.7 m^2/g versus 9.0 m^2/g respectively.

Both powders are then sintered using the same procedure. They are loaded into a 12.7 mm inner diameter graphite dies with boron nitride dry lubricant, and sintered in a hydraulic hot press at 1160 °C and 120 MPa with a linear heating rate of ∼20 °C/min and a hold time of 30 min. After sintering, the pressure is released and the system is passively cooled to room temperature over a period of a few hours. The consolidated pucks are then cut and polished for characterization. X-ray Diffraction (XRD) is performed by a PANalytical EMPYREAN diffractometer with a CuK_α source. Transmission Electron Microscopy (TEM) is performed by a Tecnai T12 and Electron Energy Loss Spectroscopy (EELS) is performed on a JEOL JEM-2100F with a Gatan Quantum SE GIF operating with

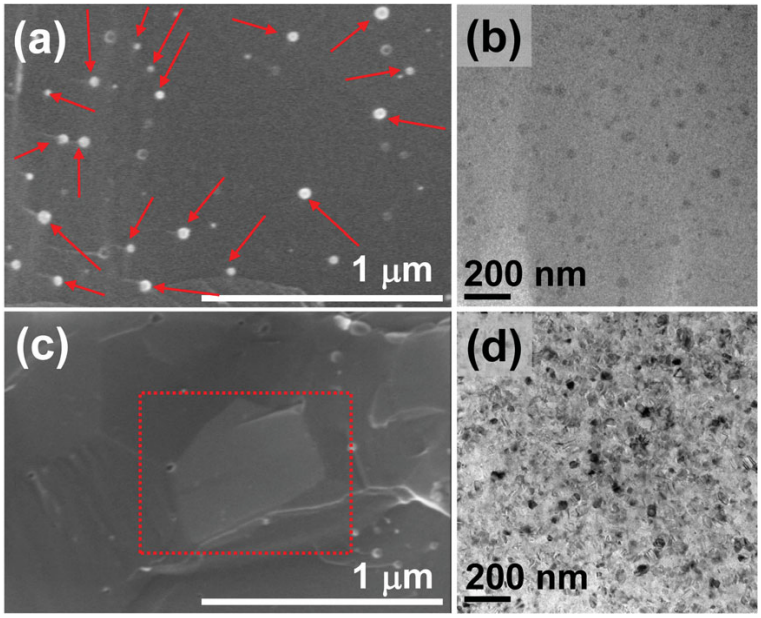

Figure 3.2: (a) Cross-sectional SEM image for the samples obtained by hot-pressing the plasma-produced particles. (b) TEM of sample obtained using the plasma-produced particles, after FIB-ing. (c) and (d) show the same analysis but for the sample produced by hot-pressing the powder obtained by ball-milling of silicon ingots.

an accelerating voltage of 200 kV. Thermoelectric characterization is performed at the Jet Propulsion Laboratory using both commercial (for thermal diffusivity) and specialized custom equipment (for electrical conductivity, carrier concentration and Seebeck coefficient), as listed below. Thermal conductivity is calculated using the thermal diffusivity measured via Laser Flash Analysis (LFA). A commercial Netzsch LFA 404 is used for the measurement. To obtain the thermal conductivity, we have used the temperature-dependent heat capacity values measured in [60]. We have performed independent differential scanning calorimetry (DSC) measurements to confirm that the heat capacities of our samples are close to the values reported in [60] (see Figure 3.3). Reports in the literature confirm that nanostructuring does not lead to deviation in the heat capacity compared to that of bulk silicon [61, 62]. The density is measured via Archimedes method and corrected for thermal expansion [63].

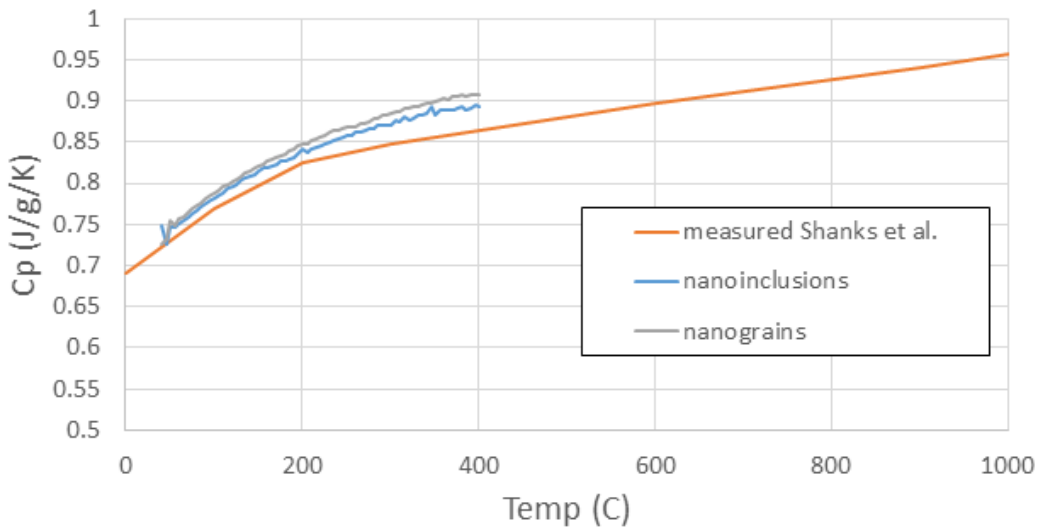

Figure 3.3: Measured heat capacity of the "nanoinclusions" and "nanograins" samples, together with the heat capacity measurement reported by Shanks et al. The heat capacity of the "nanoinclusions" and the "nanograins" samples have been measured on a Netzsch DSC 214 Polyma.

Electrical conductivity and carrier concentration are measured by high temperature Hall Effect using the 4 point probe Van der Pauw method described in details in [64]. Seebeck coefficient is measured using the system and procedure described in details in [65]. All thermoelectric measurements (thermal diffusivity, electrical conductivity, carrier concentration, Seebeck coefficient) are taken with the same heating rate of 180 K/hr to maintain consistent contributions from carrier concentration effects such as dopant precipitation.

3.3 Results and Discussion

Figure 3.2 shows SEM and TEM images for the samples after sintering. Figure 3.2(a,b) are respectively the cross-section SEM and TEM of the sample obtained by sintering the plasma-produced nanoparticles. The SEM image is acquired from a fracture surface,

and the TEM analysis is performed after focused ion beam (FIB) processing. The presence of inclusions, which we highlight with red arrows, is clear in both Figure 3.2(a,b). Grains are not clearly distinguishable in Figure 3.2(a). The lack of background contrast in Figure 3.2(b) suggests that the sample in the field of view is oriented along the same crystallographic direction. Figure 3.2(c,d) show the same analysis on the sample obtained by sintering the powder produced via ball-milling. The density of inclusions is much lower than in Figure 3.2(a), and grain boundaries (see red box) are clearly distinguishable. The TEM image in Figure 3.2(d) shows strong contrast, suggesting that the sample is composed of small domains. The XRD spectra for the two samples, not shown for brevity, are consistent with polycrystalline diamond silicon. Williamson-Hall analysis is performed by fitting the first seven diffraction peaks with a two-peaks pseudo-voigt profile to account for the $k_{\alpha 1}$ and $k_{\alpha 2}$ contributions. The analysis suggests that the sample with nanoinclusions has $\sim$3 μm crystal domain sizes, while the sample with nanograins has $\sim$200nm crystal domain sizes. This result is consistent with the results in Figure 3.2. We attribute the large grain size for the sample produced using the plasma-produced nanoparticles to the much larger surface area of this powder. The reduced activation energy for diffusion at the nanoparticle surface has been proposed as the mechanism justifying the enhanced sintering kinetics of small particles [66, 67].

We have performed electron energy loss spectroscopy (EELS) spectrum imaging on the sample shown in Figure 3.2(a,b) to better characterize the nanoinclusions. From the acquired spectrum images the counts from the oxygen and silicon K-edge were extracted, producing the images shown in Figure 3.4(a,b). This analysis indicates that the inclusions

are oxygen rich. Their composition, small size and spatial uniformity in the silicon matrix are consistent with oxide precipitates. Such structures are actually well known in silicon processing science, with early reports suggesting that oxide contamination can lead to the formation of small inclusions in silicon [68–70]. The presence of oxygen contamination in our sample is likely the result of the high-temperature in-flight treatment, which removes the hydrogen termination from the nanoparticle surface. The resulting 'bare' surface is extremely sensitive to oxidation. Although the particles are kept nominally air-free during processing, the presence of even trace amounts of oxidizing species, which is unavoidable even in a glove-box with few ppm levels of oxygen and water, is expected to lead to partial oxidation of the particles surface. In Figure 3.2(c) we show the histogram of the distances between the oxide nanoinclusions. This was obtained by measuring the nearest neighbor distance between the particles from cross-sectional SEM images such as the one shown in Figure 3.2(a). Care was taken not to double-count particle pairs. A modified Saltykov algorithm was used to convert the raw distance distribution to the three-dimensional distribution [71]. This procedure assumes that the spatial arrangement is isotropic, which based on our observation is a safe assumption.We find that the average spacing between the particles is 160 nm. Given a size of 20 nm, this implies a nanoinclusion density and volume fraction of 2×10^{14} cm^{-3} and 0.1% respectively.

From these measurements, it is clear that different powder preparation techniques lead to very different structures after hot-pressing. We should stress that we produced our best effort at doping the samples with similar amount of phosphorous. The room temperature carrier concentrations as measured via Hall Effect are 4.9×10^{20} cm^{-3} and

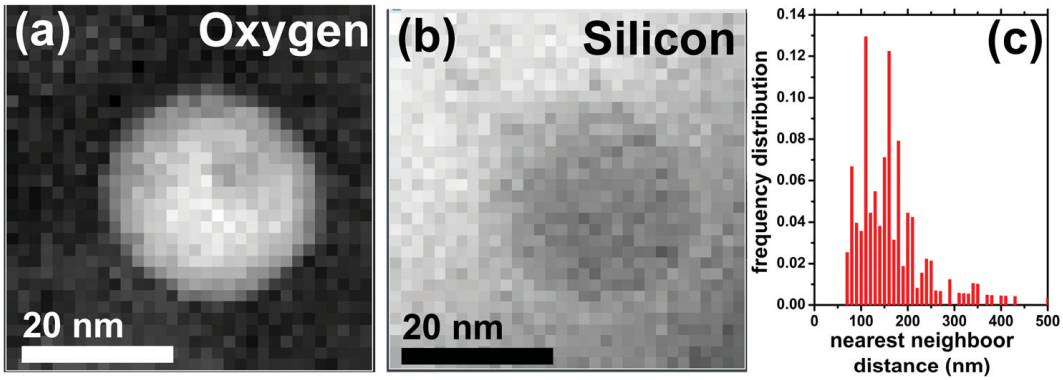

Figure 3.4: EELS-filtered TEM micrographs of the nanoinclusions. (a) Corresponds to the oxygen signal, while (b) to the silicon signal. (c) Distribution of distances between nearest neighbor inclusions.

4.5×10^{20} cm^{-3} for the 'nanoinclusions' and the 'nanograins' samples respectively. The transport properties are shown in Figure 3.5.

Despite the clear difference in nanostructure, the two samples have practically identical thermal conductivity (Figure 3.5(a)), with a minimum value of ∼12 W/mK at 1000 K. The lattice thermal conductivities for the two samples are close (inset of Figure 3.5(a)), reaching a minimum value of ∼9 W/mK at 1200 K. The electronic contribution was calculated using the Wiedermann-Franz law using a Lorenz factor equal to 2.2×10^{-8} J^2 K^{-2} C^{-2} [5]. The room temperature electrical resistivities are 4.25 $\mu\Omega$m and 5 $\mu\Omega$m for the 'nanoinclusions' and the 'nanograins' samples respectively, and the room temperature Seebeck coefficients are 60 μV/K and 78 μV/K respectively. This difference is justified by higher carrier concentration of the 'nanoinclusions' sample. The main difference between the two samples is in the temperature dependence of the electrical resistivity. For both samples, it first increases at higher temperature because of increased electron–phonon scattering, and then decreases because of the increased solubility of phosphorous in the lattice [59]. While

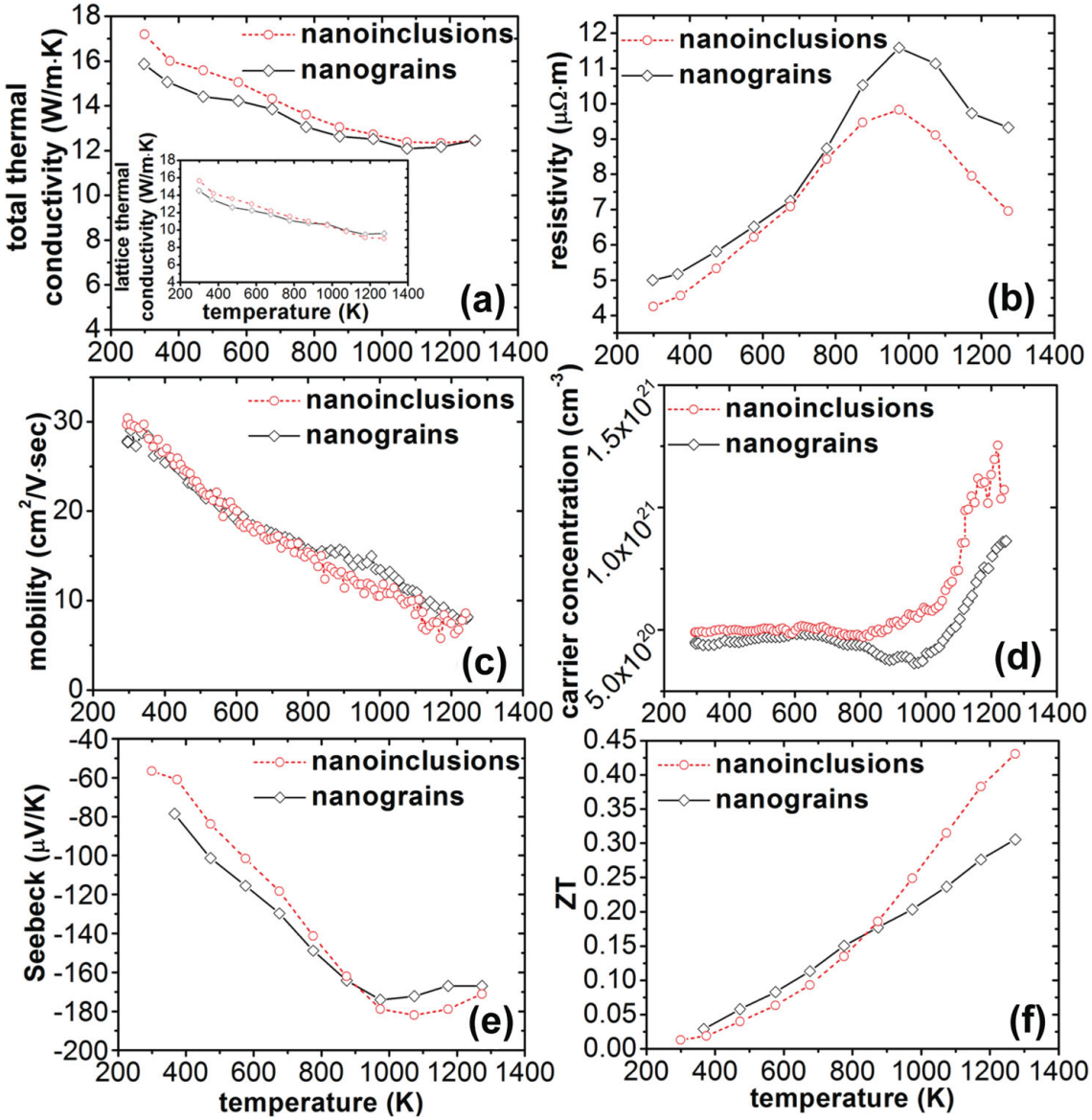

Figure 3.5: Summary of the transport properties of the samples under investigation. (a) Full and lattice thermal conductivity. (b) Electrical resistivity. (c) Charge carrier mobility. (d) Carrier concentration. (e) Seebeck coefficient. (f) Figure of merit ZT.

similar behavior has been observed in other bulk silicon samples [5, 72], the resistivity does not increase with temperature as much for the 'nanoinclusions' samples compared to the 'nanograins' sample. The difference between the two curves is significant at temperatures higher than 800 K (Figure 3.5(b)). While the mobilities are practically identical (Figure 3.5(c)), the carrier concentration dependence (Figure 3.5(d)) is quite different between the two samples. For the 'nanograins' sample, there is first a decrease in carrier concentration starting at 800 K, which is attributed to dopant precipitation effects in heavily doped silicon [5, 73], followed by an increase at 1000K due to increased solubility of phosphorous in silicon [59]. For the 'nanoinclusions' sample, the dopant precipitation effect is practically absent, and the carrier concentration starts increasing at 800 K. Two mechanisms may contribute to this difference in behavior. First, the 'nanograins' sample has a much larger density of grain boundaries compared to the 'nanoinclusions' sample, and phosphorous is well-known to segregate at boundaries in polycrystalline silicon samples [74, 75]. Second, the oxide nanoinclusions may act as a phosphorous reservoir. This is to be expected given the known capability of phosphorous-rich silica to act as a dopant source to silicon [76]. It is also important to notice that despite the larger increase in carrier concentration with temperature for the 'nanoinclusions' sample, the Seebeck coefficients remain close for the two samples (Figure 3.5(e)). This leads to an overall improvement in power factor for the 'nanoinclusions' sample. Similar improvements in power factor for samples with inclusions and precipitates have been reported for more complex chemistries. Bulk nanostructured PbSe with CdSe nanoinclusions shows an improved power factor because of the effect of the inclusions on the valence band structure [77,78].Metallic inclusions in chalcogenides also lead

to an improvement in the power factor, this time induced by energy filtering of the charge carriers [79, 80]. Similar effects may be at play in our 'nanoinclusions' sample. Overall, this results in a thermoelectric figure of merit of 0.45 at 1300K for the 'nanoinclusions' sample, considerably higher than the 0.3 at the same temperature for the 'nanograins' sample. The formation of oxide inclusion in silicon has been observed previously for samples obtained by sintering of nanoparticles with a native oxide layer [72, 81]. For these studies, the oxygen content is as high as 25% by mass, and the grain size is small (100 nm). Therefore both nanoinclusion and grain boundaries contribute to the reduction in thermal conductivity, making it difficult to separate their roles. On the other hand, our samples have been processed by avoiding air exposure as much as possible. The oxygen content is sufficiently low that it is difficult to quantify reliably via SEM-EDS. While determination of the oxygen content is challenging (extensive EELS characterization is prohibitive considering that it requires advanced sample preparation via FIB), the grain size is in our samples is large (microns). Grain boundaries are not expected to contribute significantly to the reduction in thermal transport. This study therefore provides a more direct comparison between the role of grain boundaries and nanoinclusions on transport properties.We should also stress that high ZT values have been measured on multiple samples processed identically to the one discussed earlier, as shown in Figure 3.6.

3.4 Conclusions

We have compared the thermal and charge transport properties of two samples with starkly different nanoscale structures: a sample with relatively small crystalline do-

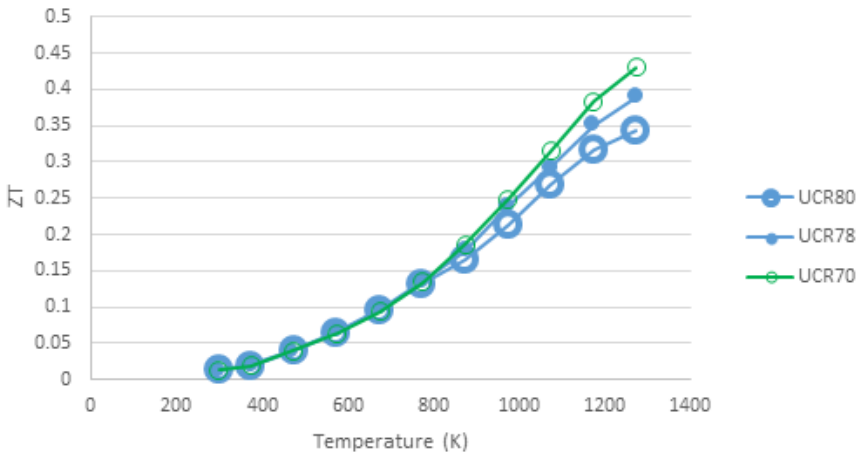

Figure 3.6: Plot of ZT as a function of temperature for 3 samples processed under conditions identical to the ones described.

mains and a sample with much larger crystals but with well-dispersed nanoinclusions. Our results suggest that nanoinclusions can be effective at scattering heat carriers (phonons), confirming that improved strategies for the reduction of heat conductivity in bulk materials are within reach, for instance by combining the use of nanograins and nanoinclusions within one sample. Most importantly, the device with nanoinclusions shows a higher power factor. Further improvements in ZT may be attainable by optimizing the doping level for the structure with nanoinclusions.

Chapter 4

Thermoelectric Performance of Silicon with Silicon Carbide Nanoinclusions

4.1 Preface

Given the benefits of the thermodynamically driven oxide precipitates discussed in Chapter 3 on thermoelectric performance, it became of interest to externally engineer nanoinclusions with finer control. The inability to influence and control their formation limited the usefulness of the study. By externally engineering new inclusions, the prospects of modulating the size, density, and potentially the distribution of such inclusions become a possibility. Thus, we utilized the non-thermal plasma system discussed in Chapter 2, in which silicon nanocrystals nucleated in a non-thermal reactor are converted to beta-phase

silicon carbide nanocrystals by exposure to a secondary non-thermal plasma containing methane gas. All credit for performing the modeling of thermoelectric performance in this section goes to Aria Hosseini and his advisor, Prof. Alex Greaney.

4.2 Introduction

Thermoelectric generators have been heavily utilized for decades in deep-space exploration as reliable, solid state power sources with very long lifetimes. [2] For these applications cost is not an issue, and so the best performing compounds are often exotic and expensive materials. However, in pursuit of energy efficiency there is an increasing desire for thermoelectric that can be used more widely in terrestrial applications for waste heat recovery in automobiles or industrial facilities. [82] In these applications the key requirements are that the materials be inexpensive, made from earth abundant and environmentally benign constituents, using process that are scalable and that produce bulk material. To meet the first of these challenges much research has been devoted to improving the performance of silicon based thermoelectric materials with the aim of exploiting both the earth abundance of silicon and technologies that have been developed over the last half century for scalable fabrication of silicon semiconductor devices.

The performance of a thermoelectric material at a given operating temperature, T, is quantified by the dimensionless of merit $ZT=(\sigma S^2\ T)/k$, where k is the total thermal conductivity, and the numerator combines the electrical transport properties of Seebeck coefficient, S, and electrical conductivity σ. Silicon is a poor thermoelectric; however, in silicon heat is conveyed primarily by phonons, and importantly, the mean free path of

phonons in bulk Si is orders of magnitude larger than the mean free path of electrons. This means that by nanostructuring devices at the scale of the phonon mean free path, one can significantly reduce the thermal conductivity while having only minor impact on electron transport properties. This strategy has been used to produce dramatic improvements in ZT of silicon based thermoelectrics.

Studies on nanoscale materials, such as thin films or nanowires, indicated that electrical and thermal conductivities could be effectively decoupled through introduction of nanoscale features to enhance ZT. [4] Studies on bulk structures have mostly been limited to grain size engineering. Modeling and computational works suggest such features are ineffective at scattering low-frequency phonons, which can carry a great amount of heat at higher temperatures. [83] Nanoinclusions and nanopores have been demonstrated as an alternative to grain reduction for achieving low thermal conductivities, and are speculated to increase the Seebeck coefficient through energy filtering of electrons. [9, 84–87]

While these works demonstrate the potential of Si as an inexpensive thermoelectric, they all rely on low dimensional geometries which make it difficult for the technology to be scaled for practical application. This chapter presents an alternate approach that uses a novel plasma synthesis approach to create a monolithic n-type Si thermoelectric that is nanostructured with a finely controlled suspension of monodispersed silicon carbide inclusions. In a further departure from the prior approaches, these inclusions not only scatter the transport of phonons, but act to enhance silicon's thermoelectric power factor, $P=\sigma S^2$, by electron energy filtering — that is, energy selective scattering of electrons. The following sections will describe the synthesis, characterization, and thermoelectric performance

of the SiC/Si composites, the theory of electron energy filtering and rationale for its exploitation for engineering improved thermoelectric performance, and a semi-classical model of the thermoelectric performance that demonstrates the observed increased power factor can only be explained through electron energy filtering. This model is then used to identify further strategies for optimizing the improvement in ZT.

4.3 Synthesis and Characterization of Si/SiC nanocomposites

Attempts to increase the phonon scattering in bulk Si by polycrystalline grain refinement have proven to be relatively unsuccessful because while it is relatively straightforward to synthesize materials with nanoscale polycrystalline grain structure, grain boundaries present limited impedance mismatch and so are ineffective at blocking the long wavelength acoustic phonons which carry the majority of the heat. [83] Introducing secondary phases is one approach for introducing scattering centers with a strong acoustic mismatch either through density difference, or as in the case of SiC and Si, by elastic modulus mismatch. The central difficulty of introducing secondary phases is in controlling the size and distribution of inclusions during the high temperature processing of the material — that is, creating a dispersion that does not interfere with the concentration dissolved dopant, and inhibiting Oswald ripening of the secondary phases. To circumvent these issues, we have developed a method for sintering Si from a precursor premixed with monodispersed SiC nanoparticles. The SiC particles were produced by the non-thermal plasma technique described in Chapter 2, which provides precise control of the particle size. The advantage

of this approach is that the Si compact can be sintered to full densification at temperatures below that at which the SiC coarsens, and so the microstructure is decoupled from the heat treatment schedule.

Parent silicon powder produced by high energy ball milling (i.e. the "nanograins" sample discussed in Chapter 3) was chosen to isolate the effects of these silicon carbide inclusions from that of the silicon oxide inclusions, as well as improve throughput time. The silicon carbide nanoparticles were mixed with the ball milled silicon powder and sintered via hot pressing.

The plasma produced SiC nanocrystals have been mechanically mixed with silicon nanopowders by these two methods at various ratios and hot-pressed into bulk pucks via conventional hot pressing. Increasing silicon carbide fraction yields significantly improved power factor and ZT through the enhancement of the Seebeck coefficient.

Parent silicon powder was prepared by sealing silicon ingot fragments, red phosphorus, and gallium phosphide in a tungsten carbide vial with 3 tungsten carbide balls of 10mm diameter in a 50 mL WC vial and Spex milling for 24 hours, similar to methods shown in ref [5]. Doping concentrations were 2.16% red phosphorus and 0.46% GaP. β phase silicon carbide nanocrystals were synthesized by a scaled up process of the two-step non-thermal plasma synthesis reactor described in Chapter 3. The silicon carbide particles are roughly spherical in shape with an average diameter of 8nm. Particle size distributions were obtained from TEM images, shown in figure 4.2b.

Silicon powders containing 0%, 1%, 5%, and 10% volume fractions of silicon carbide particles were mixed by high energy ball mill method consisted of one hour of the same spex

milling used to produce the silicon nanopowders The parent sample was doped with 2.16% red phosphorus and 0.46% GaP They were loaded into 12.7 mm inner diameter graphite dies with boron nitride dry lubricant, and sintered in a hydraulic hot press at 1160°C and 120 MPa with a linear heating rate of ∼20°C/min to 1160°C and a hold time of 30min. After sintering, the pressure was released and the system is passively cooled to room temperature over a period of a few hours. The consolidated pucks were then cut and polished for characterization.

Extensive structural and thermoelectric characterization techniques were performed on the initial powder and sintered pellets. X-ray Diffraction (XRD) was performed by a PANalytical EMPYREAN diffractometer with a CuK_{α} source. Scanning Transmission Electron Microscopy (STEM) and Energy Dispersive X-ray Spectroscopy (EDS) were performed by a Titan Themsis 300 STEM.

All thermoelectric characterization was performed at the Jet Propulsion Laboratory, using commercial equipment for thermal diffusivity and dedicated custom equipment for carrier concentration, electrical conductivity, and Seebeck coefficient. Thermal conductivity was calculated using the measured thermal diffusivity via a commercial Netzch LFA 404 Laser Flash Analysis (LFA), using density measured by Archimedes method and literature values for heat capacity and thermal expansion [63], [60][Need to format NIST-JANAF REF for SiC Cp]. The thermal conductivity was then calculated. Electrical conductivity and carrier concentration were measured by high temperature Hall Effect using a 4 point probe Van der Pauw method described in detail in [64]. Seebeck coefficient was measured by a Small ΔT Seebeck Coefficient Measurement System using the system and procedure

described in [65]. All thermoelectric measurements were taken with a heating rate of 180 K/hr to maintain consistent contributions from carrier concentration effects such as dopant precipitation, and allow for proper calculation of ZT.

Bulk samples with >99% theoretical density were achieved for the 0%, 1%, and 5% samples. The 10% sample exhibited significant porosity and only reached ∼90% theoretical density.

XRD spectra on the consolidated pucks sintered from the HE BM powder (figure 4.1) confirm β-phase SiC peak features at 35.68°, 60.04°, and 71.84° 2θ for the 1%, 5%, and 10% conditions. Scherrer first peak approximation (corrected for instrumental broadening by a LaB_6 standard) on the SiC (111) peak yields a consistent crystallite value of 8nm for all three samples. This agrees with particle size statistics from TEM and suggests that there was no grain growth in the SiC inclusions during sintering. Scherrer first peak approximation on the Si (111) peak yields crystallite sizes of 147nm, 115nm, 88nm, and 70nm for 0%, 1%, 5%, and 10% respectively. The decrease in calculated crystallite size as a function of SiC volume fraction is most likely due to broadening from SiC inclusions embedded in silicon grains, rather than an actual decrease in grain size. A minor tungsten carbide signature is present at ∼49.2°, most likely a contamination from the WC vials or balls used during the Spex milling process. As silicon carbide is harder than tungsten carbide. Some degree of this contamination is unavoidable during the high energy ball milling process.

Figure 4.2c and d show a cross-section of the 5% HE BM sample, prepared by Focused Ion Beam (FIB) and characterized by Scanning Tunneling Electron Microscopy (STEM) and Energy Dispersive X-ray Spectroscopy (EDS) on a Titan Themis 300. There

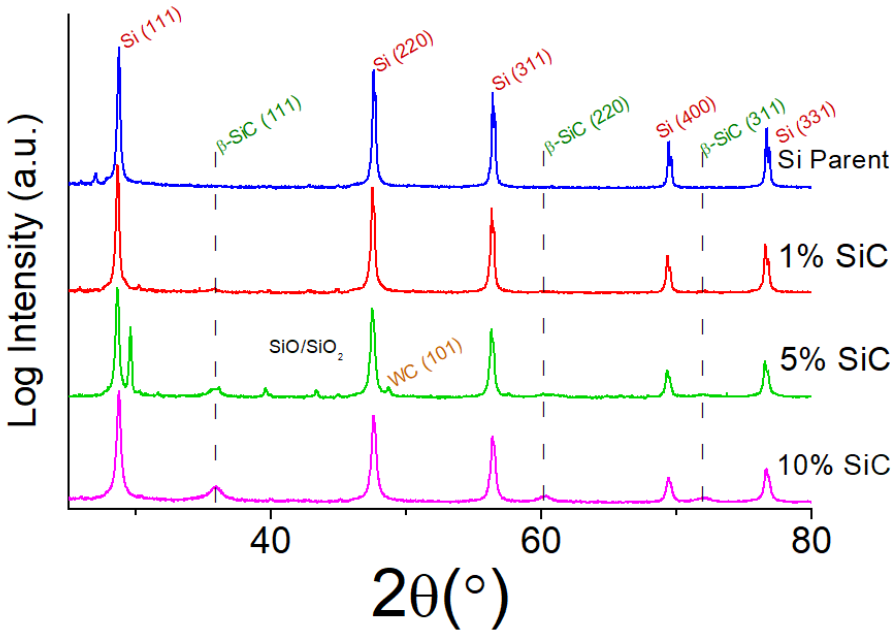

Figure 4.1: XRD of bulk composites with up to 10% volume fraction of SiC inclusions

is a significant presence of 10nm features in the STEM images. That these features line up exactly with carbon signature (green) in the EDS map confirms they are the silicon carbide nanoinclusions. These images suggest a combination of random distribution of inclusions and some clustering / segregation at grain boundaries and nanopores.

The thermoelectric properties of the 0%, 1%, and 5% samples are shown in Figure 4.3. The parent sample produced had somewhat poor thermoelectric performance (ZT = 0.19), with relatively high thermal conductivity that is attributed to abnormally large grain structure for the high energy ball milling process.

Despite this low absolute performance in the parent silicon, significant relative improvements can be readily seen from the thermoelectric data. The thermal conductiv-

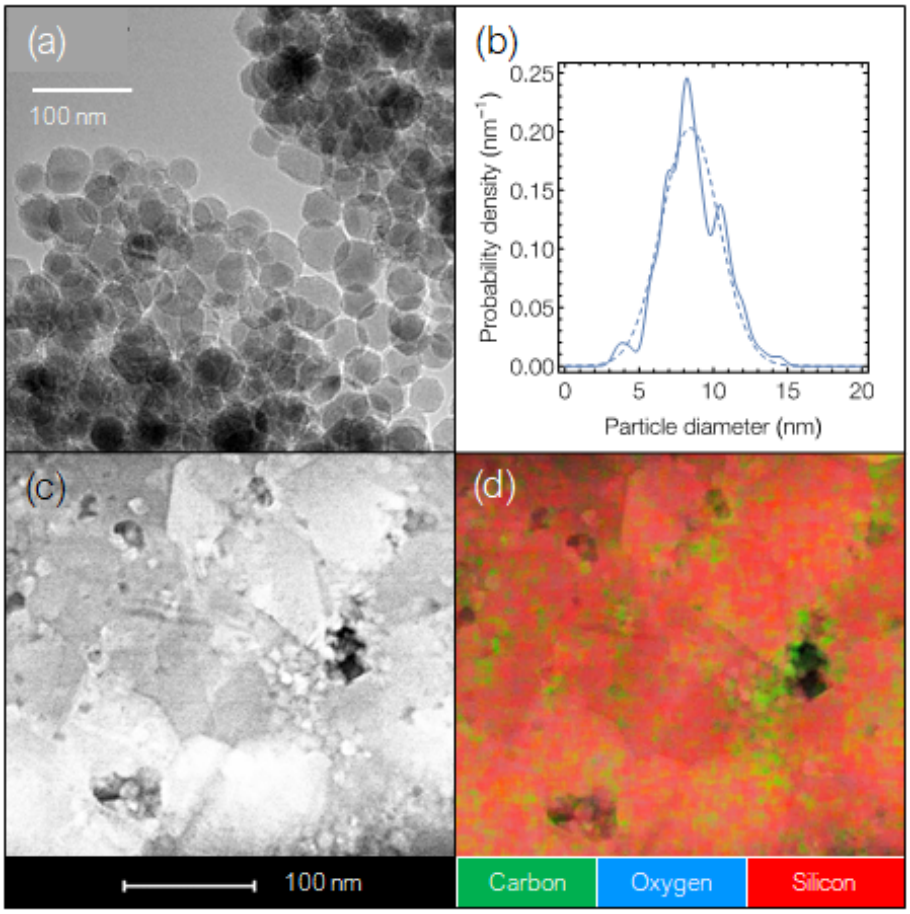

Figure 4.2: (a) TEM of the as-produced SiC powder. (b) Particle size distribution of the SiC nanoparticles (c) TEM of a section of the 5% SiC sample, prepared by FIB (d) Corresponding EDS map

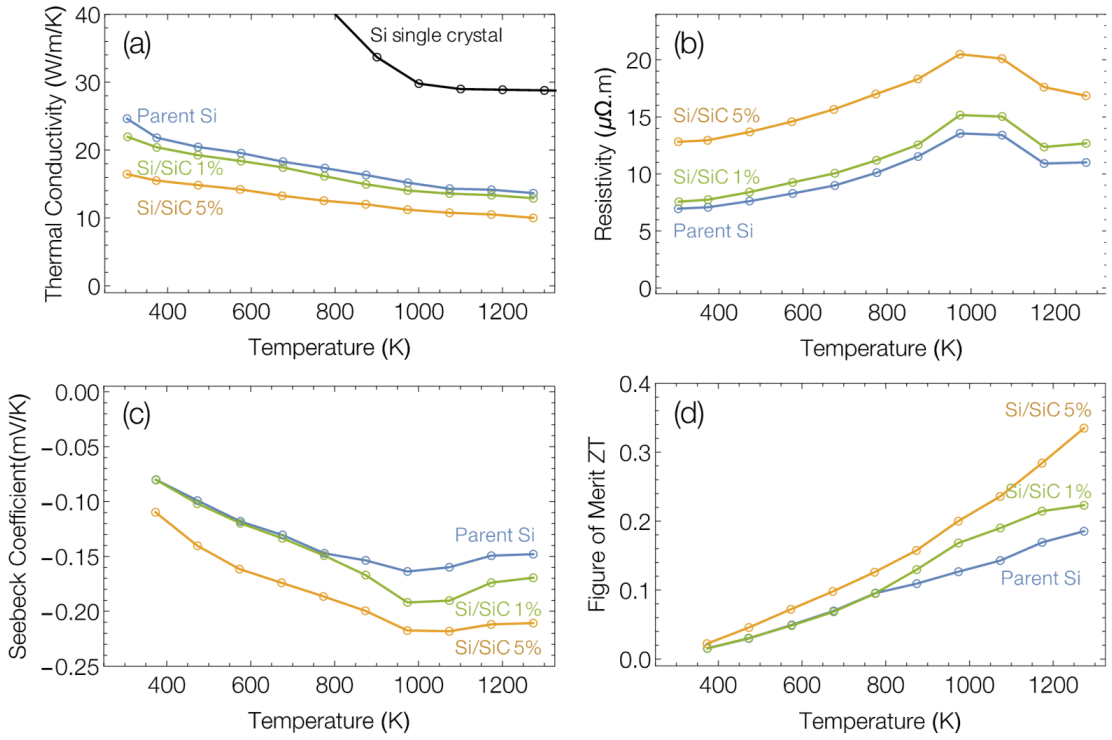

Figure 4.3: (a) Thermal conductivity (b) Electrical Resistivity (c) Seebeck Coefficient (d) Calculated ZT

ity is slightly depressed from 15 W/m*K to 10 W/m*K at 5% inclusions. However, this reduction in thermal conductivity is more than offset by a significant increase in electrical resistivity. There is also a massive increase in the magnitude of the Seebeck coefficient, increasing by as much as 40% at peak temperature. Since the S term of the equation for power factor and ZT is squared, this significant gain in Seebeck results in an impressive 80% improvement in ZT of the parent sample. The addition of undoped SiC dispersoids reduces the doping concentration in the material, which is consistent with the decreased electrical conductivity and increased Seebeck, however, this reduction alone is not sufficient to explain the magnitude by which the Seebeck coefficient is increased. We hypothesize that this gain in the power factor is due to an electron energy filtering effect from the SiC nanoinclusions. This concept will be explained in the following section, and the subsequent section presents a phenomenological model that shows electron energy filtering is required in order to quantitatively account for the the full increase in power factor.

In order to prevent the tungsten carbide contamination, the "low-energy" ball milling process was developed. This consisted of a glass jar containing 30 grams of 3mm diameter YSZ grinding media beads and a 30 RPM rock tumbler. Mixtures of 1%, 5%, and 10% silicon carbide were placed in the jar with the parent silicon and tumbled for 24 hours prior to sintering. Again, fully dense composites were achievable up to 5%, and the 10% sample did not fully densify. XRD analysis confirms there is still a small presence of SiO and SiO_2 peaks, but the WC contamination is completely gone. Additionally, the parent silicon sample is slightly better performing than that of the HE BM study (ZT of 0.3). However, the effect of the addition of silicon carbide inclusions is significantly different than

previously seen. There is still an increase in electrical resistivity, however there is almost no change in thermal conductivity, and the increase in the magnitude of the Seebeck coefficient is significantly less than before. The combination of these factors results in an identical ZT between the parent and the 5% sample.

It was hypothesized at this point that the high energy and low energy ball milling processes result in drastically different dispersions of SiC nanoinclusions: In the HE BM process, SiC particles are embedded and cold welded to both the surfaces and interiors of the larger silicon particles. Consequently, during the sintering process, SiC particles are well-distributed throughout both grains and grain boundaries. Whereas in the LE BM process, there is insufficient energy to embed the SiC particles inside of the silicon. Instead they simply decorate the surface of the silicon, resulting in most or all of the SiC particles residing at grain boundaries in the sintered bulk.

This explanation is consistent with the effects of both studies on thermal conductivity and Seebeck coefficient. In the HE BM sample, new phonon-scattering sites are introduced into the bulk of the grains. In the LE BM sample, any phonon-scattering events that would result from the SiC inclusions are already done by the grain boundary. Thus, the remainder of this chapter will focus solely on the HE BM samples.

4.4 Tuning Power Factor by Electron Energy Filtering

Thermoelectric properties of semiconductors can be derived from the semi-classical Boltzmann transport equation using single relaxation approximation integrating over a single carrier band. The electrical conductivity, σ, and Seebeck coefficient, S, at temperature

T are given by:

$$\sigma = -\frac{1}{3}e^2 \int \chi(E,T)\tau(E,T)dE \tag{4.1}$$

$$S = \frac{1}{3eT} \int \frac{\gamma(E,T)\tau(E,T)dE}{\chi(E,T)\tau(E,T)dE} \tag{4.2}$$

where e is the electron charge, and τ(E,T) is momentum relaxation time of electrons with energy E. [cite Gang Chen's book] The kernels χ and γ include all the non-scattering terms and are given by

$$\chi(E,T) = v(E)^2 \frac{df(E_f,E,T)}{dE} D(E) \tag{4.3}$$

$$\gamma(E,T) = (E - E_f)\chi(E,T) \tag{4.4}$$

Here E_f is the Fermi level, v(E) the carrier group velocity, f(E_f,E,T) the Fermi-Dirac distribution, and D(E) is density of states available for charge carriers. The kernel χ is known as the transport distribution function [88].

Engineering density of state effective mass may lead to high Seebeck coefficient. However, in most cases there is countervailing trend between S and σ by lowering the electron mobility.

Rather than engineering D(E) which is an intrinsic property of a material, one can consider engineering the energy dependence of the electron scattering time τ(E,T). This can be considered as adding additional sources of extrinsic scattering centers (a task that

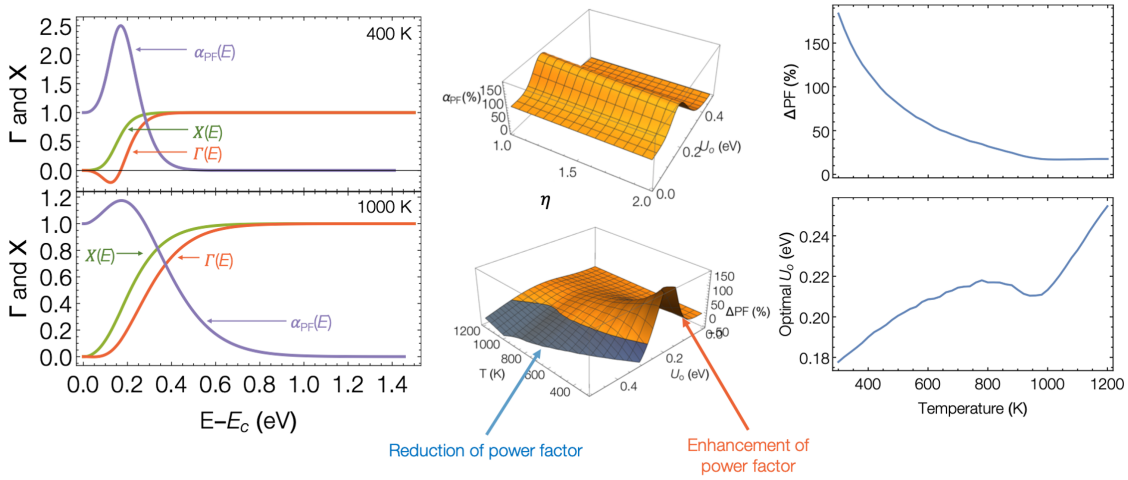

Figure 4.4: (a) Normalized X and Γ plotted at low temperature (top) and high temperature (bottom) (b) Power factor enhancement as a function of T, η, and U_0, assuming E $\propto$ K$^{\eta}$ (c) Optimal barrier height and corresponding power factor enhancement as a function fo temperature

is easier than engineering intrinsic properties) that obstruct electrons depending on their energy.

Introducing any new scattering mechanism shortens the electron relaxation time and hence reduces σ. For the Seebeck coefficient however, τ appears in both numerator and denominator of the formula for S, and consequently both numerator and denominator decreases by adding new scattering mechanism. The central concept in electron energy filtering is to introduce a scattering mechanism that can reduce the denominator in S faster than the numerator so that the overall Seebeck coefficient is increased.

Normalized χ and γ for silicon are plotted in figure REF for T=500 K (medium temperature) and T=1200 K (relatively high temperature). These functions differ only in the (E-E_f) term in γ. For n-doped semiconductors, χ is negative for any E in the conduction band, and γ is positive for electron with energy lower than E_f. The Fermi level, E_f depends

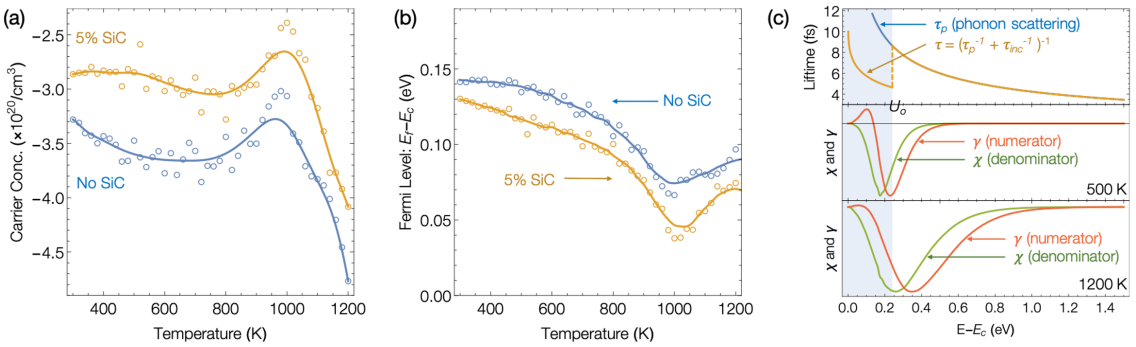

Figure 4.5: (a) Temperature dependence of experimentally measured carrier concentration (dots) and its smoothed interpolation (lines) for the P doped Si with 0% and 5% volume fraction SiC. (b) The temperature dependence of the Fermi level computed to be self-consistent with the experimental carrier concentration. (c) Energy dependence of the electron scattering time (top), including and additional filleting scattering process that is felt by all electrons with energy less than U_0. χ and γ, normalized and plotted at 500 K and 1200 K (bottom)

on the carrier concentration, which is plotted vs. temperature in Figure 4.5 for the Si with and without SiC inclusions, along with their corresponding E_f's in Figure 4.5b. E_f is above the conduction band edge, E_c, so there is a range of electron energies where γ is positive. Figure 4.5c-1 shows the electron relaxation time τ_p by phonons, which is the dominant scattering term at high temperatures. We will show by adding SiC inclusions, electrons with low energy (E< U_0) feel an extra scattering term (τ_0 in Figure 4.5c-1). This extra scattering term functions as an energy filter, such that the denominator of S reduces faster than the numerator. Consequently, S increases. We have modeled this scattering term as

$$\tau_{inc} = \frac{H(U_0 - E)}{\tau_0} \tag{4.5}$$

where H is Heaviside function and U_0 and τ_0 are used to impart extra scattering term of τ_0 to electrons with lower energy than U_0. We used Matthiessen's rule to sum this

extrinsic scattering term with electron-phonon scattering. The total relaxation time will be

$$\tau^{-1} = \tau_p^{-1} + \tau_{inc}^{-1} \tag{4.6}$$

τ is plotted in Figure 4.5c-1 for U_0=0.21 [eV] and τ_0=8 [fs]. To better understand the filtering effect, we define X(E) and Γ(E) as

$$X(E) = \frac{\int_0^E dE' \bar{\chi}(E')\tau_p(E')}{\int_0^\infty dE' \bar{\chi}(E')\tau_p(E')} \tag{4.7}$$

$$\Gamma(E) = \frac{\int_0^E dE' \bar{\gamma}(E')\tau_p(E')}{\int_0^\infty dE' \bar{\gamma}(E')\tau_p(E')} \tag{4.8}$$

Here, $\bar{\chi}$ and $\bar{\gamma}$ are normalized χ and γ, respectively. Figure REF shows these functions. X(E) is always positive, while Γ(E) is negative for E<E_A, where E_A is the energy level where$\int_{E_c}^{E_f} \bar{\gamma}$ dE = $\int_{E_f}^{E_A} \bar{\gamma}$ dE. For energies above E_A , Γ(E) is positive. Γ(E) is always less than X(E) and converges to 1 slower than X(E).

4.5 Optimization of Power Factor Enhancement

We assume the extreme case of τ_0=0. This means all the electrons with energy lower than U_0 are completely blocked. We define $\alpha_\sigma(U_0)$ and as the ratio of the materials' electrical conductivity with and without energy filtering. Similarly, we define $\alpha_\sigma(U_0)$ and $\alpha_{PF}(U_0)$.

$$\alpha_\sigma(U_0) = 1 - X(U_0) \tag{4.9}$$

$$\alpha_S(U_0) = \frac{1-\Gamma(U_0)}{1-X(U_0)} \tag{4.10}$$

$$\alpha_{PF}(U_0) = \frac{(1-\Gamma(U_0))^2}{1-X(U_0)} \tag{4.11}$$

Figure 4.5 shows these functions. As expected, α_σ is always less than 1 and reduces with increasing U_0. α_S is always more 1 which means energy selective effect improves S for all ranges of U_0. For $\tau_0 = 0$, α_σ (U_0) increases monotonically with increasing U_0, however for $\tau_0 \neq 0$, we see an extremum in Seebeck coefficient. α_{PF} (U_0) is initially above 1 but reduces to below 1 when $\Gamma(U_0)$ = 1 - $\sqrt{(1-X(U_0))}$. The optimum value of σ_{PF} (U_P^*F) satisfies the following equation

$$U_P^*F = E_f + \frac{3}{2}TeS\frac{1-\Gamma(U_P^*F)}{1-X(U_P^*F)} = E_f + \frac{3}{2}TeS\alpha_S(U_P^*F) \tag{4.12}$$

where S is the Seebeck coefficient for the no filtering case.

4.6 Engineering material properties to enhance filtering effect

A key question to answer is how to improve energy selective scattering by engineering materials properties. We assume E $\propto K^\eta$, where K is the electron wavevector. Density of state, group velocity and relaxation time can be approximated by D(E)$\propto K^2\frac{dK}{dE}$, V $\propto \nabla_K E$, and $\tau_P(E) \propto \sqrt{E}$, respectively. Therefore, $\bar{\chi} \propto E^{\frac{1}{\eta}+\frac{3}{2}}$. Using Riemann sum, we

approximate the numerator of (4.8) as:

$$\int dE\bar{\chi}(E)\frac{df}{dE} \approx \Sigma_{i=1}^{n}\frac{df\frac{E_i+E_{i-1}}{2}}{dE}\int_{E_{i-1}}^{E_i} dE\bar{\chi}(E) \tag{4.13}$$

Therefore, X(U_0) and $\Gamma(U_0)$ can be rewritten as

$$X(U_0) = \frac{\Sigma_{E<U_0}(E_i^{\frac{1}{\eta}+\frac{3}{2}} - E_{i-1}^{\frac{1}{\eta}+\frac{3}{2}})}{\Sigma_E(E_i^{\frac{1}{\eta}+\frac{3}{2}} - E_{i-1}^{\frac{1}{\eta}+\frac{3}{2}})} \tag{4.14}$$

$$\Gamma(U_0) = \frac{\frac{2\eta}{2+5\eta}\Sigma_{E<U_0}(E_i^{\frac{1}{\eta}+\frac{5}{2}} - E_{i-1}^{\frac{1}{\eta}+\frac{5}{2}}) - \frac{2\eta}{2+3\eta}\Sigma_{E<U_0}(E_i^{\frac{1}{\eta}+\frac{3}{2}} - E_{i-1}^{\frac{1}{\eta}+\frac{3}{2}})}{\frac{2\eta}{2+5\eta}\Sigma_E(E_i^{\frac{1}{\eta}+\frac{5}{2}} - E_{i-1}^{\frac{1}{\eta}+\frac{5}{2}}) - \frac{2\eta}{2+3\eta}\Sigma_E(E_i^{\frac{1}{\eta}+\frac{3}{2}} - E_{i-1}^{\frac{1}{\eta}+\frac{3}{2}})} \tag{4.15}$$

Figure 4.4 shows σ_{PF} using (4.14) as a function of both U_0 and η. For low value of U_0, increasing η decreases α. Whereas for high values of U_0, increasing η increases α. We know that the higher η is, the lighter the effective mass will be. Therefore, we predict materials with light effective mass will show more improvement in power factor with low barrier inclusions. Conversely, heavy effective mass materials perform better with high barrier.

4.7 Modeling σ and S of parent Silicon

The electronic band structure of silicon, and from it, D(E), and v(E), were computed with density functional theory (DFT) using the Vienna Ab initio Simulation Package (VASP). The calculations were performed using the generalized gradient approximation (GGA) with the Perdew-Burke-Ernzerhof exchange correlation functional (PBE). Ion cores

where represented with projector augmented wave (PAW) pseudopotentials. Calculations were performed using an energy cutoff of the basis plane waves of 700 eV and 4x4x4 k-point sampling of the Brillouin zone of Monkhorst– Pack scheme. We relaxed the cell shape and the atom positions to minimize forces to less than 10^2 eV/$\mathring{A}$. Electronic properties were computed on 12x12x12 k-point sampling of the Brillouin zone. These intrinsic materials properties were assumed to be temperature independent. The group velocity is obtained from the conduction band curvature, v=$\frac{1}{\hbar}\nabla_k E$. The Fermi energy is temperature dependent and is highly dependent on the carrier concentration, which is also seen experimentally to depend on temperature. Rather than model the physics of changes in carrier concentration with temperature, we use the empirically measured carrier concentration as an input and then compute the fermi level that is self-consistent with this carrier concentration.

At high temperatures, electron scattering is dominated by electron-phonon coupling. We model this by assuming that the scattering time from phonons, τ_p, has a power law dependence on the electron energy and temperature of the form

$$\tau_p(E) = A_0\sqrt{ET} \tag{4.16}$$

The coefficient A_0 was tuned to a value of 73.5 fs $\text{eV}^{1/2}$ $\text{K}^{1/2}$ to fit the conductivity to the experimentally measured values for σ of Si with no inclusions. Putting this form of the scattering time into the formula for the Seebeck coefficient((4.2)) A_0 cancels from the numerator and denominator leaving the model for S with no external tuning parameter. Eq. (4.1) and (4.2) are used to calculate electrical conductivity and Seebeck coefficient, respectively. The results are plotted Figure 4.3.

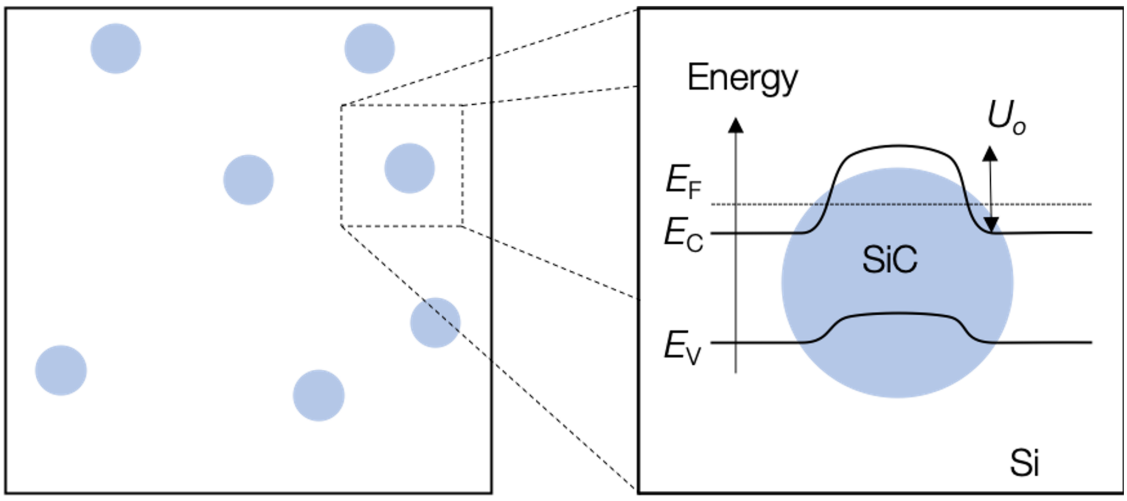

Figure 4.6: Schematic of dispersoids and bandgap offset of the Si:SiC interface

4.8 Modeling Electron Filtering from Inclusions

For Si we have a mechanistic understanding of the electron scattering and its energy dependence and hence we obtain a meaningful quantitative prediction of the transport properties. The scattering from inclusions is more complex arising from the bending of the conduction bend edge in the SiC, as shown schematically in Figure 4.6. We do not know what the band bending looks like in this region, and so we instead take a different and phenomenological approach. This model is based on the band offset between SiC and Si (2.36 eV and 1.17 eV respectively at 0 K) and the distance between inclusions. We expect that the band offset scatters low energy electrons more than high energy electrons. Equation (4.5) represents the same mechanism: The electrons with lower energy than the U_0 scatter but electrons with higher energy do not feel the inclusions. We modeled the selective scattering due to inclusions with eq (4.5). τ_0 and U_0 were tuned to 9.7 fs and 0.23 eV, respectively to fit the conductivity with experimentally measured value of σ.

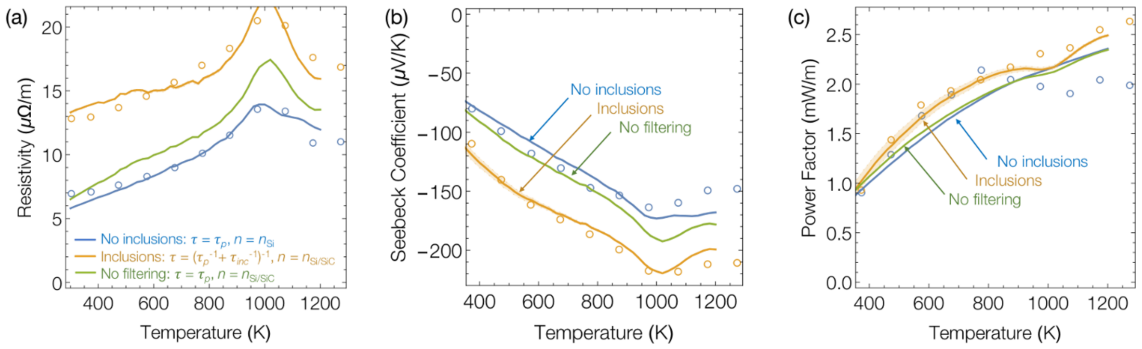

Figure 4.7: Model (lines) and Experimental (dots) of (a) resistivity (b) Seebeck (c) power factor of P doped Si with 0% (blue) and 5% (gold) volume fraction of SiC. The green lines are for the model with no inclusion scattering, but using the carrier concentration for the Si with 5% SiC

Figure 4.7 shows experimental and model predicted values of resistivity ρ, Seebeck coefficient, S, and power factor, PF for 0% and 5% volume fraction of SiC inclusions. As mentioned in the previous section, adding inclusions lowers carrier concentration. Resistivity, Seebeck, and power factor are plotted in figure for this carrier concentration with and without considering τ_{inc} (orange and green lines, respectively). These plots show that the change in carrier concentration alone does not explain the change in ρ and S, but the phenomenological energy selective scattering does. This phenomenological model should be used with caution since there is no mechanistic basis for it. Hence, we plotted uncertainty lines in the Seebeck and power factor plots.

4.9 Conclusions

We have compared the thermal and electrical transport properties of fully dense, bulk nanocomposites of up to 5% volume fraction of silicon carbide in silicon. The distribution of the externally added inclusions is not as well-dispersed as has been observed for

precipitation-driven inclusions but still has a significant impact on the transport properties. This model demonstrates that extra energy selective scattering is needed to explain the electrical transport properties of Si with 5% of SiC inclusions. We assumed a phenomenological form of the inclusion scattering, tau_inc. We observed no dependency between optimal value of PF and phenomenological parameter of τ_0 at different temperatures. We also observed a wide scope of improving PF especially at relatively low temperature. Although we cannot read too much into the physical meaning of U_0, it is worthwhile to explore the increases in power factor that would theoretically be achieved using this mechanism.

Chapter 5

Silicon Carbide Nanoparticles with Graphene-like Coatings

5.1 Introduction

Graphene is a 2D hexagonal lattice of sp^2 hybridized carbon. Ever since its initial discovery, it has attracted tremendous attention for its electrical, thermal, and optoelectronic properties. [89, 90] Three-dimensional Graphene nanostructures – sometimes called folded graphene – have been demonstrated in computational and limited experimental works to exhibit surface plasmon resonance (SPR) [91,92] Previous experimental works have achieved various nanostructures through different means. Graphene nanoribbons have been achieved via chemical synthesis or lithographic methods. [93, 94] The optoelectronic properties of such structures can be manipulated by either their structure, or through electrostatic doping. [95] Graphene sheets have been wrapped around metal oxide nanowires

and nanoparticles to form hybrid structures through a liquid phase chemical process. [96] Finally, graphene on has been grown on hexagonal-phase (6H) silicon carbide by high temperature annealing of silicon carbide micropowders. [97, 98] However, due to size effects on SPR of nanoparticles, significantly smaller particles must be realized to harness SPR in the infrared regime. [99, 100]

In this work, we demonstrate tunable infrared SPR in ceramic core, graphitic shell, hybrid nanoparticles. Silicon carbide nanoparticles with a narrow size distribution exhibiting conformal graphitic or "graphene-like" shells are synthesized by a two-step non-thermal plasma process. Silicon nanoparticles produced in a first non-thermal plasma stage are rapidly carbonized by a second non-thermal plasma into beta-phase silicon carbide nanoparticles. The process is controllable such that the surfaces can be tuned between bare silicon carbide, single layer, and few layers of graphene coating. The precise mechanism by which the graphitic layer is formed is likely the result of the chemical vapor deposition of methane onto the nanoparticle surface, which occurs at sufficiently high temperature to induce formation of graphene planes. This is consistent with the intense heating of nanoparticles in such plasmas which has been reported in several publications. [36, 45] The plasmon response of these particles in the infrared is modeled using an "Equivalent dielectric permittivity" model assuming spherical symmetry. The model has been demonstrated to be in good agreement (<10% error) to rigorous Mie Theory calculations for similar systems. [91] The sharp peaks produced by the model in ref [91] contrast with broad features seen in this experimental work. This discrepancy is reconciled by reduction of the value for graphene mobility and by weighting the results by the particle size distribution. The experimen-

tally measured peak position of the infrared plasmonic response matches closely with that predicted by the model.

5.2 Experimental

The material was produced by a nanoparticle synthesis reactor very similar to the one previously reported by in ref [101]. It is comprised of two continuous flow capacitively coupled non-thermal plasma reactors in series. Each of the plasma discharges is sustained through a copper electrode around the quartz tube, which is biased by a 13.56 MHz radio frequency power supply. The biased electrodes couple to the center grounded flange during operation. 100 standard cubic centimeters per minute (sccm) of argon containing 1.37% silane is flown through the primary plasma reactor to form silicon nanoparticles. A 2 mm diameter orifice separates the two reactors. Following the primary reactor, methane is added to the flow downstream of the orifice, and the silicon nanoparticles are carbonized in the secondary plasma to form beta phase silicon carbide nanoparticles and grow the graphitic surface. The pressure in the first reactor, in which silane is converted into silicon nanoparticles, is X Torr. The pressure in the second reactor, in which the carbonization takes place, is variable and kept at either 3 Torr or 6 Torr for the samples discussed in this contribution. Downstream of the reactors, a stainless-steel mesh collects the nanoparticles and the gas is evacuated by a roughing pump.

The produced material was analyzed by a variety of powder techniques. X-ray Diffraction was performed on a Panalytical Empyrean with a CuKα source. Raman was performed on a Horiba LabRam with a 532 nm laser excitation. Transmission Electron

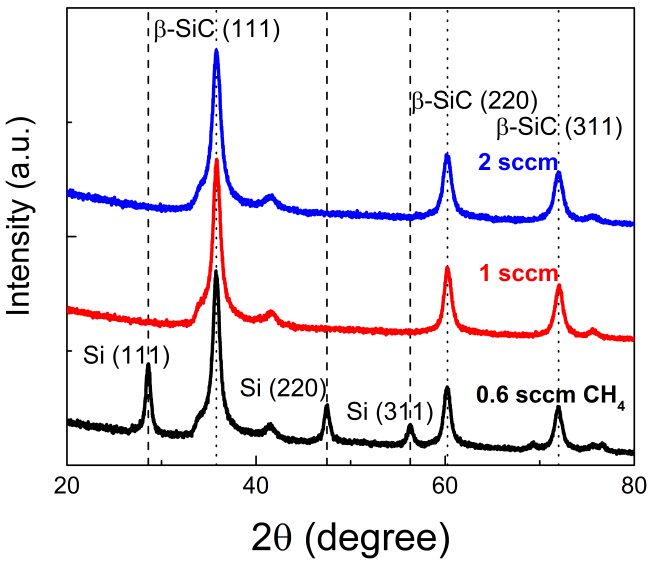

Figure 5.1: XRD spectra of the material produced as a function of increasing methane flow. The primary peaks of Silicon are indexed with dashed lines and the primary peaks of β-SiC are indexed with dotted lines.

Microscopy was performed on a Tecnai T12. Fourier Transform Infrared Spectroscopy was performed on a Nicolet iS50 with a ZnSe Attenuated Total Reflectance window.

The infrared extinction response of the material was calculated as a function of particle size and graphene mobility using the model presented by Shi et al [91], which will be discussed in detail below.

5.3 Results

Six samples were synthesized as a function of both reactor pressure and methane flow. The reactor pressure was varied between 3 and 6 torr, and the methane flow ranged from 0.6, 1, and 2 sccm. XRD is shown in Figure 5.1. Some silicon is still present at the

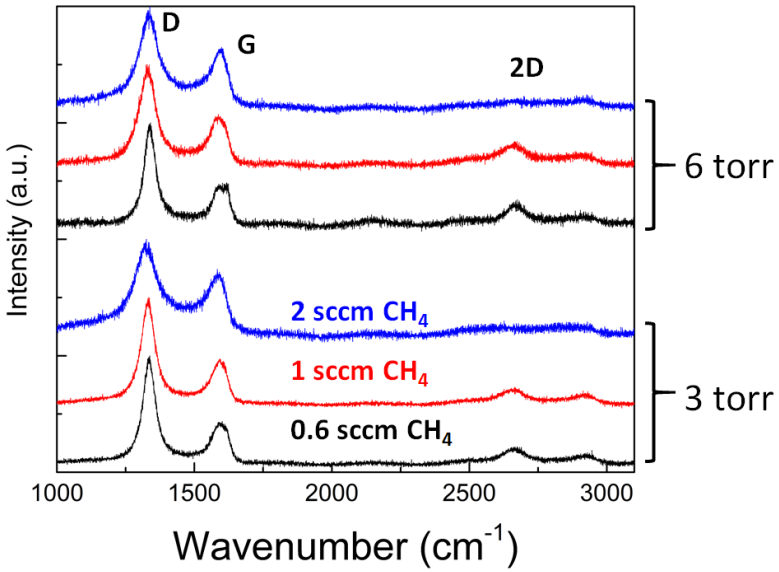

Figure 5.2: Raman spectra of the material.

lower methane flow conditions, although both Raman and TEM confirm the presence of graphitic carbon. Raman is shown in figure 5.2. For each sample, there are two clear peaks present around 1350 cm^{-1} and 1580 cm^{-1}, corresponding to the D and G bands of carbon, respectively. The D:G peak intensity ratio ranges from 1.9:1 to 3:1, indicating a mixture of disorded and graphitic material. [102] However, there is no significant peak present at the 2D position around 2700 cm^{-1}, which correlates to the presence of graphene. [103] Despite this, the signature of a graphene shell is clearly visible in the TEM (see figure 5.3). Additional TEM of each sample condition is provided in Figure S1 of the supplementary material.

The diameters of 100 particles were measured from TEM micrographs at each condition to collect particle size statistics (see Figure 5.4-insets). Particle diameter means

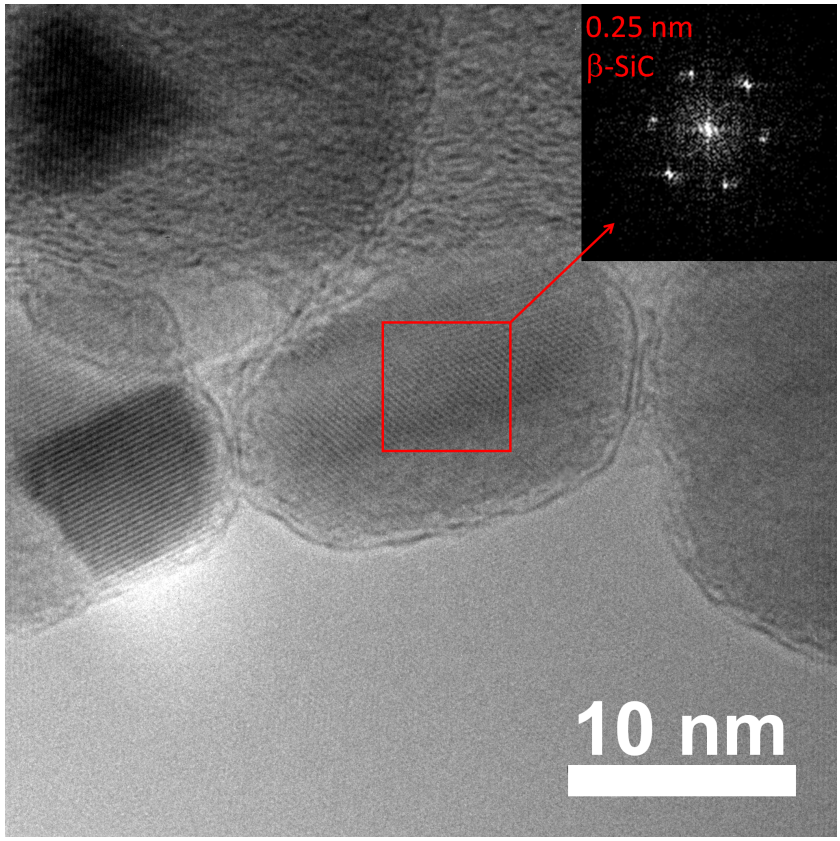

Figure 5.3: TEM of a silicon carbide particle exhibiting a graphene coating. FFT (inset) of the selected area demonstrates the material is β-SiC.

were found to be 11.5 nm and 19 nm for the 3 and 6 torr conditions. There is relatively little change in particle size as a function of methane flow. FTIR was measured by drop-casting a dispersion of particles – ultra-sonicated in chloroform – onto a ZnSe ATR window. Results of FTIR are summarized in Figure 5.4. All the spectra are normalized to the height of the peak around 900 cm^{-1}, corresponding to the vibrational mode of Si-C, [104] to account for differences in the amount of drop-casted material. Most of the samples exhibit a distinct broad absorption feature. At the higher pressure condition (i.e. larger particles), this peak position redshifts considerably from ~5000 cm^{-1} (2 μm) to ~3000 cm^{-1} (3.3 μm). With increasing methane flow, the peak initially increases in magnitude, then drops considerably and redshifts to lower energies.

5.4 Modeling

A modified version of the equivalent dielectric permittivity model developed by Shi et al [91] was invoked to theoretically reproduce the broad infrared extinction features shown in Figure 5.4. The physical model treats the material as spherical core-shell particles with a silicon carbide core and a shell of graphene. The surface plasmon resonance of the particles was excited by a plane wave light source. The nanoparticle core has a radius r_{SiC}, and graphene shell thickness T_g. Although a monolayer of graphene measures 0.34 nm in thickness, the value here is taken to be 1 nm in following with preceding computational works on optical conductivity of graphene. This accounts for inhomogeneity in the growth of graphene. [105] The dielectric constant of the silicon carbide core, ε_{SiC}, is taken to be 6.52. [106] The dielectric constant of graphene is calculated from the optical conductivity

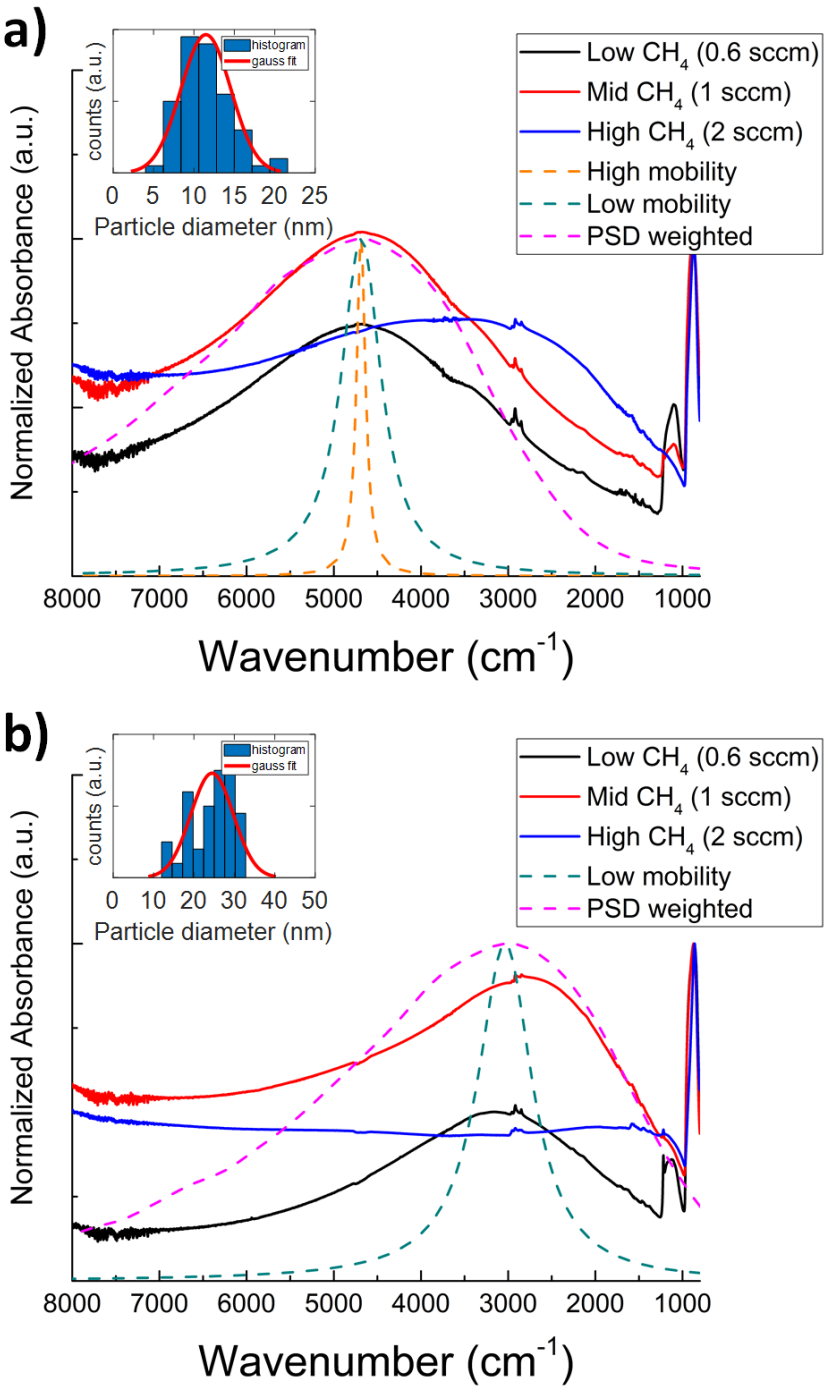

Figure 5.4: Infrared absorption of the material produced at 3 torr (top) and 6 torr (bottom). Modeled absorption spectra are represented by dashed lines. The 3 torr image (top) illustrates the effects of decreasing mobility. The dashed magenta lines are weighted the by particle size histograms (insets).

relation

$$\varepsilon_{||}(\omega) = \varepsilon_{\perp} + \frac{i\sigma_G(\omega)}{\omega\varepsilon_{\circ}T_g} \tag{5.1}$$

Where $\varepsilon_{||}$ is the in-plane dielectric constant of graphene, $\varepsilon_{\perp}$ is the out-of-plane dielectric constant of graphene (set to the value of graphite, 2.5), ω is the excitation light frequency, and $\varepsilon_{\circ}$ is the vacuum dielectric permittivity constant. The optical conductivity of graphene is calculated as follows from the random phase approximation with the local limit condition based on the Kubo formalism [107]:

$$\sigma_G = \sigma_{intra}(\omega) + \sigma_{inter}(\omega) \tag{5.2}$$

$$\sigma_{intra}(\omega) = \frac{i2e^2k_BT}{\pi\hbar^2(\omega + \tau_g^{-1})} ln\left[2cosh(\frac{E_f}{2k_BT})\right] \tag{5.3}$$

$$\sigma_{inter}(\omega) = \frac{e^2}{4\hbar}\left[\frac{1}{2} + \frac{1}{\pi}arctan\left(\frac{\hbar\omega - 2E_f}{2k_BT}\right) - \frac{i}{2\pi}ln\frac{(\hbar\omega + 2E_f)^2}{(\hbar\omega - 2E_f)^2 + 4K_B^2T^2}\right] \tag{5.4}$$

Where σ_{intra} and σ_{inter} are the intraband and interband conductivities, respectively. e is the elementary electron charge, k_B is the Boltzmann constant, $\hbar$ is the Planck constant, T is the room temperature (300K), E_f is the fermi level of graphene, and τ_g is the carrier relaxation time. Since the nanoparticles are much smaller than the order of the wavelengths of the resonant light (1-10 microns), the core-shell particle can be treated as an isotropic homogenous particle with a singular homogenous dielectric permittivity. Due to the spherical

symmetry of the particle, each field component (x, y, z) contributes equally to the dielectric permittivity, and an equivalent dielectric permittivity value can be set as:

$$\mathcal{E}_{eq-G} = \frac{1}{3}\varepsilon_{\perp} + \frac{2}{3}\varepsilon_{||} \tag{5.5}$$

The core-shell particle can then be approximated as a homogenous material by weighting by the volume fractions

$$\mathcal{E}_{np} = f \times \varepsilon_{eq-G} + (1-f) \times \varepsilon_{SiC} \tag{5.6}$$

Where ε_{np} is the equivalent dielectric of the entire core-shell material and f is the volume fraction of graphene. The absorption, scattering, and extinction cross sections may then be calculated by [92]:

$$C_{sca} = \frac{k^4}{6\pi}|\alpha^2| = \frac{8\pi}{3}k^4R^6\left|\frac{\varepsilon_c - \varepsilon_{np}}{\varepsilon_c + 2\varepsilon_{np}}\right| \tag{5.7}$$

$$C_{abs} = kIm[\alpha] = 4\pi kR^3 Im\left[\frac{\varepsilon_c - \varepsilon_{np}}{\varepsilon_c + 2\varepsilon_{np}}\right] \tag{5.8}$$

$$C_{ext} = C_{abs} + C_{sca} \tag{5.9}$$

Where k is the wave vector of the incident light and $\mathcal{E}_c$ is the permittivity of the environment, taken as unity for air.

There are a few noteworthy differences between the particles in the computational work from Shi et al [91] and the work presented here: First, the core material is SiC instead

of SiO_2, addressed by simply adjusting the dielectric constant of the core material. Second, the coating is not a perfect coating of graphene, but is more adequately described as a defective layer or few layers of graphitic "graphene-like" material. This was accounted for by reducing the mobility of the graphene dielectric from the 10,000 cm^2/Vs to 1,000 cm^2/Vs. Lastly, the synthesized SiC particles do not have a monodispersed particle size distribution. This was accounted for by calculating the absorbance over the entire range of particle sizes and weighting the results with the particle size distribution, shown in the insets of Figure 5.4. The resulting calculated absorbance features are shown in Figure 5.4 (dashed lines). The shift in peak position due to particle size effects is consistent between model and experiment. At each pressure, the peak intensity initially increased with increased methane, with no change in peak position. Then, as methane is further increased, the peak intensity drops drastically and the position redshifts significantly.

5.5 Discussion

The full conversion of silicon nanoparticles into silicon carbide nanocrystals has been discussed extensively in our previous work. [101] The low-temperature plasma process used in this study is capable of initiating the exothermic carbonization reaction, leading to the formation of crystalline silicon carbide particles. In this work, we show that it is possible to grow a graphene shell around the carbide particles by increasing the methane concentration above the amount needed to fully convert silicon into silicon carbide. The resulting core-shell structure shows a plasmon resonance in the infrared, as verified by the model discussed above. The main parameter affecting the plasmon peak position is the

particle size, which can be controlled by varying the reactor pressure. A change in pressure translates into a change in residence time in the plasma, with lower pressure resulting in a shorter residence time and smaller particles, as confirmed by TEM (see Figure S1 of the supplementary material), particles size distribution (see insets of Figure 5.4), and the IR absorption spectra (see Figure 5.4). We have also found that an increase in the methane flow rate does not lead to a significant change in plasmon peak position at first. An increase from 0.6 sccm to 1 sccm induces an increase in the absorption cross section relative to the absorption from the Si-C stretching mode at $\sim$900 cm^{-1}. TEM analysis suggests that for the lowest methane flow rate, some of the particles are not covered by a graphene coating, i.e. the sample is not functionally uniform. While it is difficult to quantify this observation by TEM, the FTIR data is consistent with an increase in the fraction of particles showing a plasmonic response. We stress that the plasmon response in Figure 5.4 is normalized over the Si-C signal which is due to the nanoparticles core. An increase in methane flow rate from 1 sccm to 2 sccm induces the weakening of the plasmonic band, its red shift and its significant broadening. TEM analysis suggests that the particles are covered by a thick graphitic carbon layer. Our interpretation is that this is due to an increase in charge carrier scattering rate, which enhances the plasmon dephasing rate and broadens absorption cross section.

The plasmon peak is quite broad even for the samples produced at 0.6 sccm and 1 sccm. In addition, the Raman spectra deviate from those that are typically reported from single- and few-layer graphene [103]. The absence of a sharp 2D feature in the Raman precludes the existence of pure or high-quality graphene coatings. This suggests that

the charge carrier scattering rate is high in these samples. TEM micrographs confirm that these graphene layer are defective. In addition, the best fit of the absorption peak profile, accounting for the particle size distribution effects, is obtained for an electron mobility value (1,000 cm^2/Vs) which is significantly lower than the best value reported for single layer graphene (10,000 cm^2/Vs). These observations suggest that coating quality needs to be further improved, for instance by applying additional annealing steps, to further increase the absorption strength and reduce the plasmon peak width. This would be desirable in applications such as chemical sensing, in which a substrate with strongly wavenumber-dependent response would increase the sensitivity of an optical detection scheme. Nevertheless, the material describe here represents the first demonstration of graphene-based plasmonic material in nanopowder form. This offers new possibilities with respect of its manipulation using well-established particle coating techniques.

5.6 Conclusion

We have demonstrated the synthesis of silicon carbide nanoparticles exhibiting graphitic coatings with reproducible and tunable SPR absorption. The broadening of the absorption features compared to previous computational works arises from the lowered mobility and the particle size distribution. The tunability of the absorption peak intensity and position was investigated and found to agree with calculations done by the equivalent dielectric permittivity model. Further improvements, in particular with respect of the particle size distribution and of the quality of the graphene layers, will allow achieving a narrower and more tunable plasmonic response. Its nanoparticle format makes this material partic-

ularly promising from the point of view of handling and ease of integration into functional structures.

Bibliography

[1] Mildred S. Dresselhaus, Gang Chen, Ming Y. Tang, Ronggui Yang, Hohyun Lee, Dezhi Wang, Zhifeng Ren, Jean Pierre Fleurial, and Pawan Gogna. New directions for low-dimensional thermoelectric materials. *Advanced Materials*, 19(8):1043–1053, 2007.

[2] D. M. Rowe. Applications of nuclear-powered thermoelectric generators in space. *Applied Energy*, 40(4):241–271, 1991.

[3] S. B. Riffat and Xiaoli Ma. Thermoelectrics: A review of present and potential applications. *Applied Thermal Engineering*, 23(8):913–935, 2003.

[4] Christopher J. Vineis, Ali Shakouri, Arun Majumdar, and Mercouri G. Kanatzidis. Nanostructured thermoelectrics: Big efficiency gains from small features. *Advanced Materials*, 22(36):3970–3980, 2010.

[5] Sabah K. Bux, Richard G. Blair, Pawan K. Gogna, Hohyun Lee, Gang Chen, Mildred S. Dresselhaus, Richard B. Kaner, and Jean Pierre Fleurial. Nanostructured bulk silicon as an effective thermoelectric material. *Advanced Functional Materials*, 19(15):2445–2452, 2009.

[6] Yuping He, Davide Donadio, Joo Hyoung Lee, Jeffrey C. Grossman, and Giulia Galli. Thermal transport in nanoporous silicon: Interplay between disorder at mesoscopic and atomic scales. *ACS Nano*, 5(3):1839–1844, 2011.

[7] R Venkatasubramanian, E Siivola, T Colpitts, and B O'Quinn. Thin-film thermoelectric devices with high room-temperature figures of merit. *Nature*, 413(6856):597–602, 2001.

[8] Alexander A. Balandin and Olga L. Lazarenkova. Mechanism for thermoelectric figure-of-merit enhancement in regimented quantum dot superlattices. *Applied Physics Letters*, 82(3):415–417, 2003.

[9] B. Lorenzi, D. Narducci, R. Tonini, S. Frabboni, G. C. Gazzadi, G. Ottaviani, N. Neophytou, and X. Zianni. Paradoxical Enhancement of the Power Factor of Polycrystalline Silicon as a Result of the Formation of Nanovoids. *Journal of Electronic Materials*, 43(10):3812–3816, 2014.

[10] J Casady and R. W. Johnson. Status of silicon carbide (SiC) as a wide-bandgap semiconductor for high-temperature applications : a review. *Solid-State Electronics*, 39(10):1409–1422, 1996.

[11] L. Hoffmann, G. Ziegler, D. Theis, and C. Weyrich. Silicon carbide blue light emitting diodes with improved external quantum efficiency. *Journal of Applied Physics*, 53(10):6962–6967, 1982.

[12] W. Münch, W. Kürzinger, and I. Pfaffeneder. Silicon carbide light-emitting diodes with epitaxial junctions. *Solid State Electronics*, 19(10):871–874, 1976.

[13] J Edmond, H Kong, A Suvorov, D Waltz, and C Carter. 6H-Silicon Carbide Light Emitting Diodes and UV Photodiodes. *Physica Status Solidi (a)*, pages 187–194, 1997.

[14] M. Boutonnet Kizling and P Stenius. Characterization and catalytic activity of silicon carbide powder as catalyst support in exhaust catalysts. *Applied Catalysis B, Environmental*, 1(3):149–168, 1992.

[15] Y. T. Yang, K. L. Ekinci, X. M H Huang, L. M. Schiavone, M. L. Roukes, C. A. Zorman, and M. Mehregany. Monocrystalline silicon carbide nanoelectromechanical systems. *Applied Physics Letters*, 78(2):162–164, 2001.

[16] Mehran Mehregany, C. A. Zorman, Narayanan Rajan, and Chien Hung Wu. Silicon Carbide Microsystems for Harsh Environments. *IEEE*, 86(8), 1998.

[17] F Huisken, B Kohn, R Alexandrescu, S Cojocaru, A Crunteanu, G Ledoux, and C Reynaud. Epitaxial Growth of B-Doped Si on Si (100) by ECR Ar Plasma CVD in a SiH 4 -B 2 H 6 -H 2 Gas Mixture without Substrate Heating. *Journal of Nanoparticle Research*, pages 293–303, 1999.

[18] N. P. Rao, N. Tymiak, J. Blum, A. Neuman, H. J. Lee, S. L. Girshick, P. H. McMurry, and J. Heberlein. Hypersonic plasma particle deposition of nanostructured silicon and silicon carbide. *Journal of Aerosol Science*, 29(5-6):707–720, 1998.

[19] N. Rao, S. Girshick, J. Heberlein, P. McMurry, S. Jones, D. Hansen, and B. Micheel. Nanoparticle formation using a plasma expansion process. *Plasma Chemistry and Plasma Processing*, 15(4):581–606, 1995.

[20] F. Vivet, A. Bouchoule, and L. Boufendi. Synthesis and characterization of SiC:H ultrafine powder generated in an argon-silane-methane low-pressure radio-frequency discharge. *Journal of Applied Physics*, 83(12):7474–7481, 1998.

[21] G Viera, J Costa, P Roura, and E Bertran. High nucleation rate in pure SiC nanometric powder by a combination of room temperature plasmas and post-thermal treatments. *Diamond and Related Materials*, 8:364–368, 1999.

[22] L. Mangolini, E. Thimsen, and U. Kortshagen. High-yield plasma synthesis of luminescent silicon nanocrystals. *Nano Letters*, 5(4):655–659, 2005.

[23] Lorenzo Mangolini. Synthesis, properties, and applications of silicon nanocrystals. *Journal of Vacuum Science & Technology B, Nanotechnology and Microelectronics: Materials, Processing, Measurement, and Phenomena*, 31(2):020801, 2013.

[24] Uwe Kortshagen. Nonthermal plasma synthesis of semiconductor nanocrystals. *Journal of Physics D: Applied Physics*, 42(11), 2009.

[25] Ryan Gresback, Tomohiro Nozaki, and Ken Okazaki. Synthesis and oxidation of luminescent silicon nanocrystals from silicon tetrachloride by very high frequency nonthermal plasma. *Nanotechnology*, 22(30), 2011.

[26] Ajay Kumar, Pin Ann Lin, Albert Xue, Boyi Hao, Yoke Khin Yap, and R. Mohan Sankaran. Formation of nanodiamonds at near-ambient conditions via microplasma dissociation of ethanol vapour. *Nature Communications*, 4:1–8, 2013.

[27] Rohan P. Chaukulkar, Koen De Peuter, Paul Stradins, Svitlana Pylypenko, Jacob P. Bell, Yongan Yang, and Sumit Agarwal. Single-step plasma synthesis of carbon-coated silicon nanoparticles. *ACS Applied Materials and Interfaces*, 6(21):19026–19034, 2014.

[28] Yadong Yin, Robert M Rioux, Can K Erdonmez, Steven Hughes, Gabor A Somorjai, A Paul Alivisatos, Chih Chen, and K. N. Tu. Formation of hollow nanocrystals through the nanoscale Kirkendall effect. *Science (New York, N.Y.)*, 304(5671):711–4, 2004.

[29] Ozgul Yasar-Inceoglu, Thomas Lopez, Ebrahim Farshihagro, and Lorenzo Mangolini. Silicon nanocrystal production through non-thermal plasma synthesis: A comparative study between silicon tetrachloride and silane precursors. *Nanotechnology*, 23(25), 2012.

[30] Z Iqbal and S Veprek. Journal of Physics C : Solid State Physics Related content Raman scattering from hydrogenated microcrystalline and amorphous silicon Raman scattering from hydrogenated microcrystalline and amorphous silicon. *J. Phys. C: Solid State Physics*, 15:377–392, 1982.

[31] A. C. Ferrari and J. Robertson. Interpretation of Raman Spectra of disorded and amorphous carbon. *Physical Review B*, 61, 1999.

[32] A. C. Ferrari and J. Robertson. Resonant Raman Spectroscopy of Disorded, Amorphous, and Diamondlike carbon. *New Zealand Dental Journal*, 64, 2001.

[33] Dengyuan Song, Eun Chel Cho, Gavin Conibeer, Yidan Huang, Chris Flynn, and Martin A. Green. Structural characterization of annealed Si1-x Cx /SiC multilayers targeting formation of Si nanocrystals in a SiC matrix. *Journal of Applied Physics*, 103(8), 2008.

[34] Y Inoue, S Nakashima, and A Mitsuihi. Raman Spectra of Amorphous SiC. *Solid State Communications*, 48(12):1071–1075, 1983.

[35] S Nakashima and H Harima. Raman Inverstigation of SiC Polytypes. *Physica Status Solidi (a)*, 162:39–64, 1997.

[36] Thomas Lopez and Lorenzo Mangolini. On the nucleation and crystallization of nanoparticles in continuous-flow nonthermal plasma reactors. *Journal of Vacuum Science & Technology B, Nanotechnology and Microelectronics: Materials, Processing, Measurement, and Phenomena*, 32(6):061802, 2014.

[37] Laurence Latu-Romain, Maelig Ollivier, Arnaud Mantoux, Geoffroy Auvert, Odette Chaix-Pluchery, Eirini Sarigiannidou, Edwige Bano, Bernard Pelissier, Charbel Roukoss, Hervé Roussel, Florian Dhalluin, Bassem Salem, Nikoletta Jegenyes, Gabriel Ferro, Didier Chaussende, and Thierry Baron. From Si nanowire to SiC nanotube. *Journal of Nanoparticle Research*, 13(10):5425–5433, 2011.

[38] C. H. Pai, K. Koumoto, S. Takeda, and H. Yanagida. Preparation of SiC hollow particles by gas-phase reaction in the SiH4-CH4-H2system. *Journal of Materials Science*, 24(10):3679–3685, 1989.

[39] R.C. Newman and J. Wakefield. The diffusivity of carbon in silicon. *Journal of Physics and Chemistry of Solids*, 19(3-4):230–234, 1961.

[40] J. M. Fairfield and B. J. Masters. Self-diffusion in intrinsic and extrinsic silicon. *Journal of Applied Physics*, 38(8):3148–3154, 1967.

[41] P Dunbar. A Model for Silicon Self-Diffusion in Silicon Carbide: Anti-Site Defect Motion. *Journal of the American Ceramic Society*, 69(2):C–33–C–35, 1986.

[42] Kenneth T. Koga, Micheal J. Walter, Eizo Nakamura, and Katsura Kobayashi. Carbon self-diffusion in a natural diamond. *Physical Review B - Condensed Matter and Materials Physics*, 72(2):8–11, 2005.

[43] H Kroger, C Ronning, H Hofsass, P Neumaier, S Bergmaier, L Gorgens, and G Dollinger. Diffusion in diamond-like carbon. *Diamond and Related Materials*, 12(November):2042–2050, 2003.

[44] J. C. Slater. Atomic radii in crystals. *The Journal of Chemical Physics*, 41(10):3199–3204, 1964.

[45] Lorenzo Mangolini and Uwe Kortshagen. Selective nanoparticle heating: Another form of nonequilibrium in dusty plasmas. *Physical Review E - Statistical, Nonlinear, and Soft Matter Physics*, 79(2):1–8, 2009.

[46] N. J. Kramer, R. J. Anthony, M. Mamunuru, E. S. Aydil, and U. R. Kortshagen. Plasma-induced crystallization of silicon nanoparticles. *Journal of Physics D: Applied Physics*, 47(7), 2014.

[47] Thomas Lopez and Lorenzo Mangolini. Low activation energy for the crystallization of amorphous silicon nanoparticles. *Nanoscale*, 6(3):1286–1294, 2014.

[48] M. S. Dresselhaus, G Dresselhaus, X Sun, Z Zhang, S. B. Cronin, and T Koga. Low Dimensional Thermoelectric Materials. *Physics of the solid state*, 41(5), 1999.

[49] Mona Zebarjadi, Giri Joshi, Gaohua Zhu, Bo Yu, Austin Minnich, Yucheng Lan, Xiaowei Wang, Mildred Dresselhaus, Zhifeng Ren, and Gang Chen. Power factor enhancement by modulation doping in bulk nanocomposites. *Nano Letters*, 11(6):2225–2230, 2011.

[50] Giri Joshi, Hohyun Lee, Yucheng Lan, Xiaowei Wang, Gaohua Zhu, Dezhi Wang, Ryan W. Gould, Diana C. Cuff, Ming Y. Tang, Mildred S. Dresselhaus, Gang Chen, and Zhifeng Ren. Enhanced thermoelectric figure-of-merit in nanostructured p-type silicon germanium bulk alloys. *Nano Letters*, 8(12):4670–4674, 2008.

[51] B. Poudel, Q. Hao, Y. Ma, Y. Lan, Austin Minnich, Bo Yu, X. Yan, Dezhi Wang, A. Muto, Daryoosh Vashaee, X. Chen, J. Liu, Mildred S. Dresselhaus, Gang Chen, and Zhifeng Ren. High-Thermoelectric Performance of Nanostructured Bismuth Antimony Telluride Bulk Alloys. *Science*, 320(5876):634–638, 2008.

[52] Zhaojie Wang, Joseph E. Alaniz, Wanyoung Jang, Javier E. Garay, and Chris Dames. Thermal conductivity of nanocrystalline silicon: Importance of grain size and frequency-dependent mean free paths. *Nano Letters*, 11(6):2206–2213, 2011.

[53] Lina Yang and Austin J. Minnich. Thermal transport in nanocrystalline Si and SiGe by ab initio based Monte Carlo simulation. *Scientific Reports*, 7(February):1–11, 2017.

[54] Nils Petermann, Niklas Stein, Gabi Schierning, Ralf Theissmann, Benedikt Stoib, Martin S. Brandt, Christian Hecht, Christof Schulz, and Hartmut Wiggers. Plasma synthesis of nanostructures for improved thermoelectric properties. *Journal of Physics D: Applied Physics*, 44(17), 2011.

[55] D. Schwesig, G. Schierning, R. Theissmann, N. Stein, N. Petermann, H. Wiggers, R. Schmechel, and D. E. Wolf. From nanoparticles to nanocrystalline bulk: Percolation effects in field assisted sintering of silicon nanoparticles. *Nanotechnology*, 22(13), 2011.

[56] Asuka Miura, Shu Zhou, Tomohiro Nozaki, and Junichiro Shiomi. Crystalline-Amorphous Silicon Nanocomposites with Reduced Thermal Conductivity for Bulk Thermoelectrics. *ACS Applied Materials and Interfaces*, 7(24):13484–13489, 2015.

[57] Ozgul Yasar-Inceoglu and Lorenzo Mangolini. Characterization of Si-Ge alloy nanocrystals produced in a non-thermal plasma reactor. *Materials Letters*, 101:76–79, 2013.

[58] U. Kortshagen and U. Bhandarkar. Modeling of particulate coagulation in low pressure plasmas. *Physical Review E - Statistical Physics, Plasmas, Fluids, and Related Interdisciplinary Topics*, 60(1):887–898, 1999.

[59] Rw Olesinski, N Kanani, and Gj Abbaschian. The P Si (Phosphorus-Silicon) system. *Journal of Phase Equilibria*, 6(2):130–133, 1985.

[60] H. R. Shanks, P. D. Maycock, P. H. Sidles, and G. C. Danielson. Thermal conductivity of silicon from 300 to 1400 K. *Physical Review*, 130(5):1743–1748, 1963.

[61] Tania Claudio, Gabi Schierning, Ralf Theissmann, Hartmut Wiggers, Helmut Schober, Michael Marek Koza, and Raphaël P. Hermann. Effects of impurities on the lattice dynamics of nanocrystalline silicon for thermoelectric application. *Journal of Materials Science*, 48(7):2836–2845, 2013.

[62] Tania Claudio, Niklas Stein, Daniel G. Stroppa, Benedikt Klobes, Michael Marek Koza, Petra Kudejova, Nils Petermann, Hartmut Wiggers, Gabi Schierning, and Raphaël P. Hermann. Nanocrystalline silicon: Lattice dynamics and enhanced thermoelectric properties. *Physical Chemistry Chemical Physics*, 16(47):25701–25709, 2014.

[63] C. A. Swenson. Recommended Values for the Thermal Expansivity of Silicon from 0 to 1000 K. *Journal of Physical and Chemical Reference Data*, 12(2):179–182, 1983.

[64] Kasper A. Borup, Eric S. Toberer, Leslie D. Zoltan, George Nakatsukasa, Michael Errico, Jean Pierre Fleurial, Bo B. Iversen, and G. Jeffrey Snyder. Measurement of the electrical resistivity and Hall coefficient at high temperatures. *Review of Scientific Instruments*, 83(12), 2012.

[65] C. Wood, D. Zoltan, and G. Stapfer. Measurement of Seebeck coefficient using a light pulse. *Review of Scientific Instruments*, 56(5):719–722, 1985.

[66] H. -JOACHIM MÖLLER and GERHARD WELSCH. Sintering of Ultrafine Silicon Powder. *Journal of the American Ceramic Society*, 68(6):320–325, 1985.

[67] C. GRESKOVICH and J. H. ROSOLOWSKI. Sintering of Covalent Solids. *Journal of the American Ceramic Society*, 59(7-8):336–343, 1976.

[68] W. Kaiser. Electrical and optical properties of heat-treated silicon. *Physical Review*, 105(6):1751–1756, 1957.

[69] Gudrun Kissinger, Dawid Kot, Jaroslaw Dabrowski, Vladimir Akhmetov, Andreas Sattler, and Wilfried Von Ammon. Analysis of the Nucleation Kinetics of Oxide Precipitates in Czochralski Silicon. *ECS Transactions*, 16(6):97–108, 2008.

[70] A Borghesi, B Pivac, A Sassella, and A Stella. Oxygen precipitation in silicon. *Lecture Notes in Physics*, 77, 1995.

[71] Homer D. Lewis, Kenneth L. Walters, and K. Allan Johnson. Particle size distribution by area analysis: Modifications and extensions of the Saltykov method. *Metallography*, 6(2):93–101, 1973.

[72] G. Schierning, R. Theissmann, N. Stein, N. Petermann, A. Becker, M. Engenhorst, V. Kessler, M. Geller, A. Beckel, H. Wiggers, and R. Schmechel. Role of oxygen on microstructure and thermoelectric properties of silicon nanocomposites. *Journal of Applied Physics*, 110(11), 2011.

[73] Cronin B. Vining. A model for the high-temperature transport properties of heavily doped n-type silicon-germanium alloys. *Journal of Applied Physics*, 69(1):331–341, 1991.

[74] J. H. Rose and R. Gronsky. Scanning transmission electron microscope microanalytical study of phosphorus segregation at grain boundaries in thin-film silicon. *Applied Physics Letters*, 41(10):993–995, 1982.

[75] Mohammad M. Mandurah, Krishna C. Saraswat, C. Robert Helms, and Theodore I. Kamins. Dopant segregation in polycrystalline silicon. *Journal of Applied Physics*, 51(11):5755–5763, 1980.

[76] B. Hartiti, A. Slaoui, J. C. Muller, R. Stuck, and P. Siffert. Phosphorus diffusion into silicon from a spin-on source using rapid thermal processing. *Journal of Applied Physics*, 71(11):5474–5478, 1992.

[77] Li Dong Zhao, Shiqiang Hao, Shih Han Lo, Chun I. Wu, Xiaoyuan Zhou, Yeseul Lee, Hao Li, Kanishka Biswas, Timothy P. Hogan, Ctirad Uher, C. Wolverton, Vinayak P. Dravid, and Mercouri G. Kanatzidis. High thermoelectric performance via hierarchical compositionally alloyed nanostructures. *Journal of the American Chemical Society*, 135(19):7364–7370, 2013.

[78] Gangjian Tan, Li Dong Zhao, Fengyuan Shi, Jeff W. Doak, Shih Han Lo, Hui Sun, Chris Wolverton, Vinayak P. Dravid, Ctirad Uher, and Mercouri G. Kanatzidis. High thermoelectric performance of p-type SnTe via a synergistic band engineering and nanostructuring approach. *Journal of the American Chemical Society*, 136(19):7006–7017, 2014.

[79] J. Martin, Li Wang, Lidong Chen, and G. S. Nolas. Enhanced Seebeck coefficient through energy-barrier scattering in PbTe nanocomposites. *Physical Review B - Condensed Matter and Materials Physics*, 79(11):1–5, 2009.

[80] Dong Kyun Ko, Yijin Kang, and Christopher B. Murray. Enhanced thermopower via carrier energy filtering in solution-processable Pt-Sb2Te3 nanocomposites. *Nano Letters*, 11(7):2841–2844, 2011.

[81] Nils Petermann, Julia Stötzel, Niklas Stein, Victor Kessler, Hartmut Wiggers, Ralf Theissmann, Gabi Schierning, and Roland Schmechel. Thermoelectrics from silicon nanoparticles: the influence of native oxide. *The European Physical Journal B*, 88(6):163, 2015.

[82] Jean-Pierre Fleurial, Alex Borshchevsky, and Thierry Caillat. New thermoelectric materials and devices for terrestrial power generators. *Space technology and applications international forum (STAIF - 97)*, 293(1997):293–298, 1997.

[83] D A Young and H J Maris. Lattice-dynamical calculation of the Kapitza resistance between fcc lattices. 40(15), 1989.

[84] Marc T Dunham, Bruno Lorenzi, Sean C Andrews, Aditya Sood, Mehdi Asheghi, Dario Narducci, E Goodson, Marc T Dunham, Bruno Lorenzi, Sean C Andrews, Aditya Sood, Mehdi Asheghi, Dario Narducci, and Kenneth E Goodson. polysilicon thin films Enhanced phonon scattering by nanovoids in high thermoelectric power factor polysilicon thin films. 253104, 2016.

[85] Atta U. Khan, Kazuaki Kobayashi, Dai Ming Tang, Yusuke Yamauchi, Kotone Hasegawa, Masanori Mitome, Yanming Xue, Baozhen Jiang, Koichi Tsuchiya, Dmitri Golberg, Yoshio Bando, and Takao Mori. Nano-micro-porous skutterudites with 100% enhancement in ZT for high performance thermoelectricity. *Nano Energy*, 31(July 2016):152–159, 2017.

[86] Hohyun Lee, Daryoosh Vashaee, D Z Wang, Mildred S Dresselhaus, and Z F Ren. Effects of nanoscale porosity on thermoelectric properties of SiGe. pages 1–7, 2010.

[87] D Coleman, T Lopez, S Exarhos, M Mecklenburg, S Bux, and L Mangolini. Thermoelectric performance of silicon with oxide nanoinclusions. 6(8):419–425, 2018.

[88] T. J. Scheidemantel, C. Ambrosch-Draxl, T. Thonhauser, J. V. Badding, and J. O. Sofo. Transport coefficients from first-principles calculations. *Physical Review B*, 68(12):125210, 2003.

[89] Matthew Allen, Vincent Tung, and Richard Kaner. Honeycomb carbon – A study of graphene. *American Chemical Society*, 110:132–145, 2010.

[90] Alexander A Balandin, Suchismita Ghosh, Wenzhong Bao, Irene Calizo, Desalegne Teweldebrhan, Feng Miao, and Chun Ning Lau. Superior Thermal Conductivity of Single-Layer Graphene. *Nano Letters*, 8(3):902–907, 2008.

[91] Zhe Shi, Yang Yang, Lin Gan, and Zhi Yuan Li. Broadband tunability of surface plasmon resonance in graphene-coating silica nanoparticles. *Chinese Physics B*, 25(5), 2016.

[92] Thomas Christensen, Antti Pekka Jauho, Martijn Wubs, and N. Asger Mortensen. Localized plasmons in graphene-coated nanospheres. *Physical Review B - Condensed Matter and Materials Physics*, 91(12), 2015.

[93] Li Zhang, Hongjie Dai, Sangwon Lee, Xinran Wang, and Xiaolin Li. Chemically Derived, Ultrasmooth Graphene Nanoribbon Semiconductors. *Science*, 319(5867):1229–1232, 2008.

[94] Melinda Y. Han, Barbaros Özyilmaz, Yuanbo Zhang, and Philip Kim. Energy bandgap engineering of graphene nanoribbons. *Physical Review Letters*, 98(20):1–4, 2007.

[95] Jianing Chen, Michela Badioli, Pablo Alonso-González, Sukosin Thongrattanasiri, Florian Huth, Johann Osmond, Marko Spasenović, Alba Centeno, Amaia Pesquera, Philippe Godignon, Amaia Zurutuza Elorza, Nicolas Camara, F. Javier García de Abajo, Rainer Hillenbrand, and Frank H. L. Koppens. Optical nano-imaging of gate-tunable graphene plasmons. *Nature*, pages 3–7, 2012.

[96] Weiwei Zhou, Jixin Zhu, Chuanwei Cheng, Jinping Liu, Huanping Yang, Chunxiao Cong, Cao Guan, Xingtao Jia, Hong Jin Fan, Qingyu Yan, Chang Ming Li, and Ting Yu. A general strategy toward graphene@metal oxide core-shell nanostructures for high-performance lithium storage. *Energy and Environmental Science*, 4(12):4954–4961, 2011.

[97] Kaixing Zhu, Liwei Guo, Jingjing Lin, Weichang Hao, Jun Shang, Yuping Jia, Lianlian Chen, Shifeng Jin, Wenjun Wang, and Xiaolong Chen. Graphene covered SiC powder as advanced photocatalytic material. *Applied Physics Letters*, 100(2), 2012.

[98] Wei Lu, Da Wang, Liwei Guo, Yuping Jia, Manping Ye, Jiao Huang, Zhilin Li, Yuan Peng, Wenxia Yuan, and Xiaolong Chen. Bipolar Carrier Transfer Channels in Epitaxial Graphene/SiC Core-Shell Heterojunction for Efficient Photocatalytic Hydrogen Evolution. *Advanced Materials*, 27(48):7986–7991, 2015.

[99] Stephan Link and Mostafa A El-sayed. Shape and size dependence of radiative, non-radiative and photothermal properties of gold nanocrystals. *Reviews in Physical Chemistry*, 19(3):409–453, 2000.

[100] Vincenzo Amendola, Osman M. Bakr, and Francesco Stellacci. A study of the surface plasmon resonance of silver nanoparticles by the discrete dipole approximation method: Effect of shape, size, structure, and assembly. *Plasmonics*, 5(1):85–97, 2010.

[101] Devin Coleman, Thomas Lopez, Ozgul Yasar-Inceoglu, and Lorenzo Mangolini. Hollow silicon carbide nanoparticles from a non-thermal plasma process. *Journal of Applied Physics*, 117(19):0–7, 2015.

[102] F. C. Tai, S. C. Lee, J. Chen, C. Wei, and S. H. Chang. Multipeak fitting analysis of Raman spectra on DLCH film. *Journal of Raman Spectroscopy*, 40(8):1055–1059, 2009.

[103] A. C. Ferrari, J. C. Meyer, V. Scardaci, C. Casiraghi, M. Lazzeri, F. Mauri, S. Piscanec, D. Jiang, K. S. Novoselov, S. Roth, and A. K. Geim. Raman spectrum of graphene and graphene layers. *Physical Review Letters*, 97(18):1–4, 2006.

[104] X Li, W Cai, J An, S Kim, J Nah, D Yang, R Piner, A Velamakanni, I Jung, E Tutuc, S Banerjee, L Colombo, and R Ruoff. Large-Area Synthesis of High-Quality and Uniform Graphene Films on Copper Foils. *Science*, 324, 2009.

[105] Naresh K. Emani, Ting Fung Chung, Xingjie Ni, Alexander V. Kildishev, Yong P. Chen, and Alexandra Boltasseva. Electrically tunable damping of plasmonic resonances with graphene. *Nano Letters*, 12(10):5202–5206, 2012.

[106] P. T. B. Shaffer and R. G. Naum. Refractive index and dispersion of Beta Silicon Carbide. *Journal of Optical Society of America*, 59:1498, 1969.

[107] E. H. Hwang and S. Das Sarma. Dielectric function, screening, and plasmons in two-dimensional graphene. *Physical Review B - Condensed Matter and Materials Physics*, 75(20):1–6, 2007.

[108] Y. Ward, R. J. Young, and R. A. Shatwell. Application of Raman microscopy to the analysis of silicon carbide monofilaments. *Journal of Materials Science*, 39(22):6781–6790, 2004.

[109] Jianing Chen, Michela Badioli, Pablo Alonso-González, Sukosin Thongrattanasiri, Florian Huth, Johann Osmond, Marko Spasenović, Alba Centeno, Amaia Pesquera, Philippe Godignon, Amaia Zurutuza Elorza, Nicolas Camara, F. Javier García de Abajo, Rainer Hillenbrand, and Frank H. L. Koppens. Optical nano-imaging of gate-tunable graphene plasmons. *Nature*, pages 3–7, 2012.

[110] Kaixing Zhu, Liwei Guo, Jingjing Lin, Weichang Hao, Jun Shang, Yuping Jia, Lianlian Chen, Shifeng Jin, Wenjun Wang, and Xiaolong Chen. Graphene covered SiC powder as advanced photocatalytic material. *Applied Physics Letters*, 100(2), 2012.

[111] Matthew Allen, Vincent Tung, and Richard Kaner. Honeycomb carbon – A study of graphene. *American Chemical Society*, 110:132–145, 2010.

[112] Li Zhang, Hongjie Dai, Sangwon Lee, Xinran Wang, and Xiaolin Li. Chemically Derived, Ultrasmooth Graphene Nanoribbon Semiconductors. *Science*, 319(5867):1229–1232, 2.

[113] Wei Lu, Da Wang, Liwei Guo, Yuping Jia, Manping Ye, Jiao Huang, Zhilin Li, Yuan Peng, Wenxia Yuan, and Xiaolong Chen. Bipolar Carrier Transfer Channels in Epitaxial Graphene/SiC Core-Shell Heterojunction for Efficient Photocatalytic Hydrogen Evolution. *Advanced Materials*, 27(48):7986–7991, 2015.

[114] Melinda Y. Han, Barbaros Özyilmaz, Yuanbo Zhang, and Philip Kim. Energy band-gap engineering of graphene nanoribbons. *Physical Review Letters*, 98(20):1–4, 2007.

[115] Claire Berger, Zhimin Song, Tianbo Li, Xuebin Li, Asmerom Y. Ogbazghi, Rui Feng, Zhenting Dai, N. Alexei, Marchenkov Edward H. Conrad, Phillip N. First, and Walt A. De Heer. Ultrathin epitaxial graphite: 2D electron gas properties and a route toward graphene-based nanoelectronics. *Journal of Physical Chemistry B*, 108(52):19912–19916, 2004.

[116] Weiwei Zhou, Jixin Zhu, Chuanwei Cheng, Jinping Liu, Huanping Yang, Chunxiao Cong, Cao Guan, Xingtao Jia, Hong Jin Fan, Qingyu Yan, Chang Ming Li, and Ting Yu. A general strategy toward graphene@metal oxide core-shell nanostructures for high-performance lithium storage. *Energy and Environmental Science*, 4(12):4954–4961, 2011.

[117] Claire Berger, Zhimin Song, Tianbo Li, Xuebin Li, Asmerom Y. Ogbazghi, Rui Feng, Zhenting Dai, N. Alexei, Marchenkov Edward H. Conrad, Phillip N. First, and Walt A. De Heer. Ultrathin epitaxial graphite: 2D electron gas properties and a route toward graphene-based nanoelectronics. *Journal of Physical Chemistry B*, 108(52):19912–19916, 2004.

[118] W. A. de Heer, C. Berger, M. Ruan, M. Sprinkle, X. Li, Y. Hu, B. Zhang, J. Hankinson, and E. Conrad. Large area and structured epitaxial graphene produced by confinement controlled sublimation of silicon carbide. *Proceedings of the National Academy of Sciences*, 108(41):16900–16905, 2011.

[119] N. J. Shaw and A. H. Heuer. On particle coarsening during sintering of silicon. *Acta Metallurgica*, 31(1):55–59, 1983.